Volume 30
DOE/DP40200-46

LLE Review

Quarterly Report

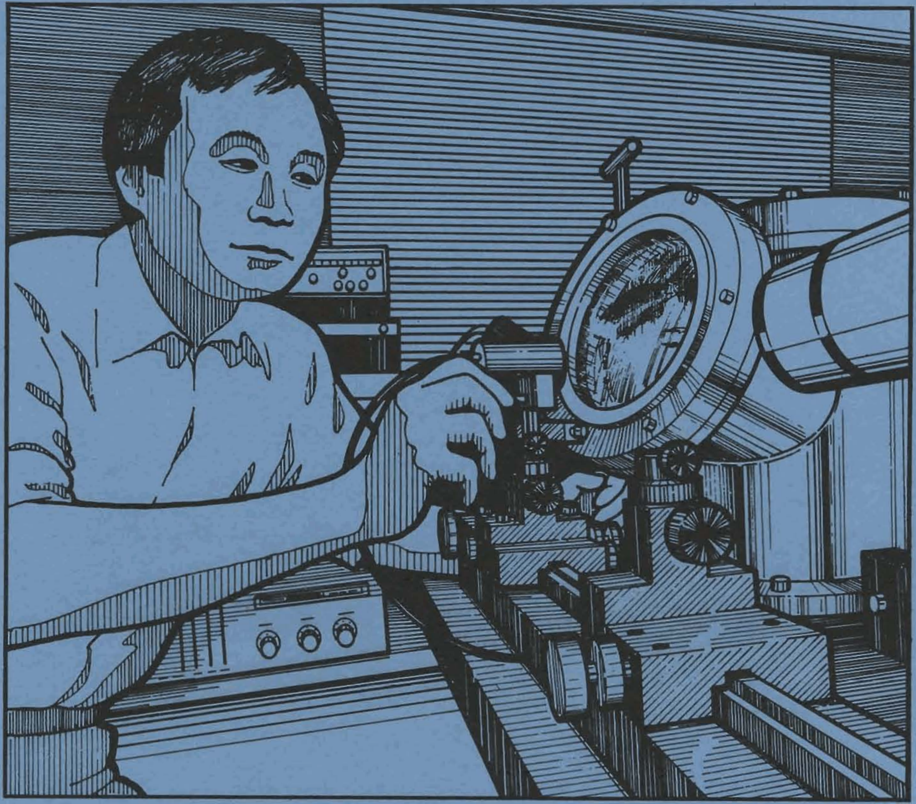

January–March 1987

Laboratory for Laser Energetics
College of Engineering and Applied Science
University of Rochester
250 East River Road
Rochester, New York 14623-1299

Volume 30
DOE/DP40200-46

LLE Review

Quarterly Report

Editor: J. Delettrez
(716) 275-5374

January–March 1987

Laboratory for Laser Energetics
College of Engineering and Applied Science
University of Rochester
250 East River Road
Rochester, New York 14623-1299

This report was prepared as an account of work conducted by the Laboratory for Laser Energetics and sponsored by Empire State Electric Energy Research Corporation, General Electric Company, New York State Energy Research and Development Authority, Ontario Hydro, the University of Rochester, the U.S. Department of Energy, and other United States government agencies.

Neither the above named sponsors, nor any of their employees, makes any warranty, expressed or implied, or assumes any legal liability or responsibility for the accuracy, completeness, or usefulness of any information, apparatus, product, or process disclosed, or represents that its use would not infringe privately owned rights.

Reference herein to any specific commercial product, process, or service by trade name, mark, manufacturer, or otherwise, does not necessarily constitute or imply its endorsement, recommendation, or favoring by the United States Government or any agency thereof or any other sponsor.

Results reported in the LLE Review should not be taken as necessarily final results as they represent active research. The views and opinions of authors expressed herein do not necessarily state or reflect those of any of the above sponsoring entities.

IN BRIEF

This volume of the LLE Review, covering the period January–March 1987, contains an improved x-ray microscopy technique for characterization of inertial fusion targets; improvements in the coefficient for inverse bremsstrahlung laser absorption; an analysis of new geometries for x-ray laser studies and the results of inertial experiments; and the National Laser Users Facility activities for this period. Finally, the laser activities on GDL and OMEGA are summarized.

The following are highlights of the research reports contained in this issue:

- The x-ray microradiography technique for the characterization of inertial fusion targets has been improved through the use of a laser-produced plasma as an x-ray source. This new method has extended the resolution to which layer thicknesses can be measured to 0.4 μm.
- The logarithmic factor in the classical coefficients for inverse-bremsstrahlung absorption of laser light has been derived to take into account the high electron density conditions near the critical surface of a target irradiated with 351-nm laser light. Comparison with previously used models shows variations of 20 to 50%.
- New geometries have been proposed for x-ray laser studies; they include two exploding foils, two ablating slabs, and a pair of exploding/ablating foils. Simulation and experimental results show higher electron density in the lasing region and improved transverse electron density profiles.

CONTENTS

Hyo-gun Kim, senior scientist and group leader of target fabrication, is making adjustments to a parylene coating chamber in which ablation layers are deposited onto inertial fusion targets.

Section 1
PROGRESS IN LASER FUSION

1.A X-Ray Microscopy of Inertial Fusion Targets Using a Laser-Produced Plasma as an X-Ray Source

Introduction

Currently, targets for direct-drive inertial fusion (IF) consist of glass microballoons that are filled with an equimolar ratio of the hydrogen isotopes deuterium and tritium (DT), and are overcoated with metallic x-ray signature layers and/or a plastic ablation layer. High spherical symmetry and an extremely smooth (<1-μm) surface finish are required for successful implosion of the laser-driven IF target. With the use of submicron laser light to drive the implosion, these target parameters become especially stringent, i.e., the nonuniformities approach the laser wavelength itself.

In the past, a major perturbation in the implosion uniformity has been the drawn-glass capillary on which the IF target is mounted. X-ray pinhole camera images have clearly demonstrated the need to eliminate the stalk mounting because it is a channel for energy to leave the imploding target. The advent of submicron stalks such as spiderweb filaments[1] reduced this perturbation in many instances. However, ablation layer coatings could still not be performed in many cases with web-mounted microballoons because, upon being coated, the diameter of the stalk would increase by twice the thickness of the plastic coating.

With the introduction of the bouncing-pan parylene coating process,[2] the stalk perturbation has been eliminated. In this process, the filled glass or plastic microballoons are bounced on an aluminum cylinder, with a pan-shaped end surface resonating at one of its natural longitudinal frequencies. The microballoons are bathed in a weak plasma to eliminate static charge buildup, which causes the extremely low-mass targets to stick to the pan. Using this technique, the IF targets can be coated with parylene without being supported and web mounted.

Several major drawbacks exist with this technique. The precharacterized microballoons lose their individual identity through the mixing that occurs during bouncing. Also, any particulate present in the pan during the coating procedure is collected by the targets and incorporated into the plastic coating. Therefore, recharacterization must be performed to determine the original parameters of each target, along with the coating uniformity and surface quality.

Several characterization techniques have been used in the past for IF targets, but few are suited for this purpose. For example, optical interferometry is limited to the characterization of transparent materials, but metal- and/or parylene-coated targets are either opaque or translucent at best. Another technique, scanning electron microscopy, is a destructive technique when used to determine coating thicknesses. Perhaps the most suitable technique for the recharacterization of bounce-coated microballoons is soft x-ray contact microradiography.[3]

X-ray microradiography has been described and utilized to characterize targets for several years by laboratories conducting IF experiments.[4] The process is capable of characterizing multilayered opaque IF targets with ease. The x-ray energy used can be specifically tailored to increase the contrast between the materials under examination. Also, x-ray microradiography is a batch characterization technique, capable of examining tens of targets in a single exposure. A typical image produced using this technique is shown (enlarged) in Fig. 30.1(a). The glass wall of the microballoon is the distinct white ring inside the lighter gray outline of the plastic coating. Various defects are made quite observable using this technique. For example, an enlargement of a surface defect evident in the outer rim of another image is given in Fig. 30.1(b).

It is clear from the enlarged image that the resolution limit of the x-ray contact microradiography technique is the grain size of the photographic emulsion used to create the original image. In the case of the Kodak 649-F plate used here, the grain size of the emulsion is of the order of 0.5 μm; therefore, the minimum feature size that may be observed would have to be as large as several grains, i.e., 1 to 2 μm. Although the grain size limitation can be alleviated to some extent through the use of digital image processing,[5] the microradiography technique is limited in that it cannot be used to measure submicron features.

In this article, we describe a soft x-ray contact microscopy technique that is inherently capable of submicron resolution. The process, a hybrid of contact x-ray microradiography and x-ray lithography,

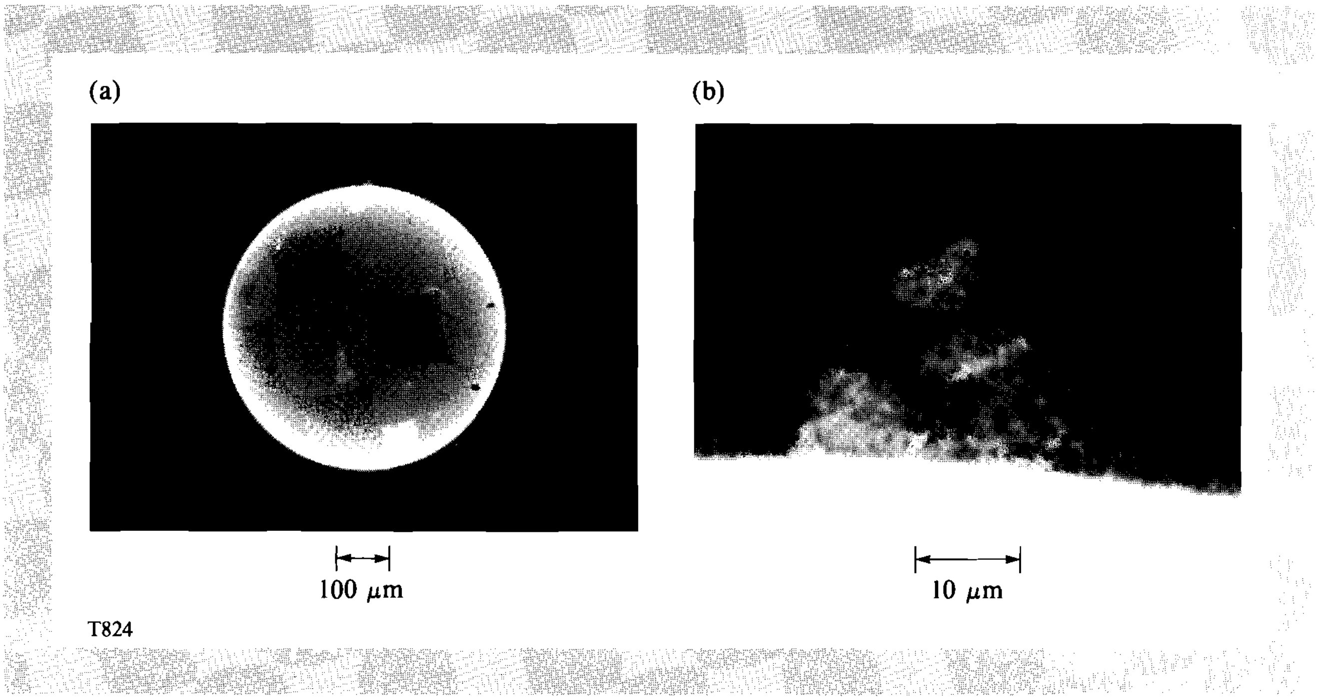

Fig. 30.1
(a) X-ray microradiograph of a plastic-coated glass microballoon.
(b) X-ray microradiograph of a surface defect in the plastic coating on a glass microballoon.

employs an x-ray sensitive photoresist as the recording medium. First developed for biological cell morphological characterization,[6] the process has been adapted here for use as a target characterization scheme by using a laser-produced plasma as an x-ray source.

Background

Images of x-ray lithographic masks with a resolution of tens of nanometers have been recorded using the x-ray resist polymethyl methacrylate (PMMA).[7] The resolution of a photoresist is inversely proportional to its sensitivity. Hence, the more sensitive resist poly(butene-1-sulfone) (PBS) was used in this experiment because the intensity of our laser-produced plasma x-ray source is insufficient to expose PMMA properly.

Contact x-ray microscopy is an improvement of conventional soft x-ray contact microradiography. A specimen is held in intimate contact with a polymer photoresist and is irradiated at normal incidence with soft x rays. The resist suffers different degrees of local radiation damage in direct proportion to the x-ray transmittance of the specimen's structure. The molecular weight of the resist is therefore locally decreased, causing an increased solubility of that region in an appropriate solvent. Upon development, the surface of the resist represents a two-dimensional topographic map of the three-dimensional specimen's density distribution.

Soft x-ray contact microscopy has undergone much development in past years in biological cell morphology and cell chemical composition determination.[8] Due to the shorter wavelength of x rays, better resolution than light microscopy can be obtained. However, this technique cannot match the resolution of the scanning electron microscope.

The x-ray source used in previous soft x-ray microscopy work was either a stationary target or synchrotron radiation.[9] Both the stationary target source and the more intense and tunable synchroton source have the disadvantage of emitting a continuous flux of x rays. Thus, any vibration in the imaging apparatus or change in the sample would blur the resulting image of the specimen.

A pulsed x-ray source is desirable for most soft x-ray microscopy work. One such source, the gas puff *z*-pinch,[10] has been proven to be less than an optimum x-ray source. A laser-produced plasma as an x-ray source has recently been demonstrated in several papers.[11] Source characteristics of laser-produced plasma x-rays, such as very small size, subnanosecond pulse duration, and tunability of wavelength, are the properties most desirable for x-ray lithography, and are not available from any other type of source. The x-ray flux has been shown to be sufficient to produce a relief image in many photoresist materials. The sensitivity of some x-ray resists was found to be one order of magnitude higher than the sensitivity published when a laser-produced plasma was used in place of conventional x-ray sources.[12]

Experimental

A schematic of the experimental configuration is shown in Fig. 30.2. The photoresist, which was filtered to 0.2-μm maximum particulate size upon shipment, was dispensed directly from the bottle and spin coated onto silicon wafer substrates to yield a film thickness of approximately 0.5 μm. This thickness was determined using thickness versus spin-rate curves supplied by the PBS manufacturer.[13] (Thicker films may be desirable to maximize the x-ray dose absorbed in the resist; however, as in photographic emulsions, a loss in resolution may result from the use of excessively thick resist films.) The coated substrates were then prebaked at 120°C for one hour to eliminate any residual solvent present in the resist film and to promote adhesion to the silicon substrate. The photoresist-coated wafer was then held in intimate contact with the CH-coated IF targets, which were supported between two tensioned, 2-μm-thick polyester films. A 2-μm-thick polyester film coated with 1000 Å of aluminum was placed between this assembly and the plasma x-ray source to filter out radiation with wavelengths longer than those of the soft x-rays. Earlier experiments had shown an intense background overexposure that had produced only a shadow of the IF target, thus overwhelming the internal structure of the target made visible by soft x rays. Filtration eliminated the previously encountered long-wavelength background exposure, and the image produced was solely due to soft x-ray exposure.

To create the x-ray-emitting plasmas, the frequency-doubled GDL (Nd:glass laser) operating at a 1-ns pulse duration with a wavelength of 534 nm was focused to a 100-μm-diameter spot onto a metal foil target. The target chamber, which contained the imaging assembly, was evacuated to a background pressure of the order of 10^{-6} torr. The microscopy setup was placed at a distance of 10 cm from and directly facing the laser target, and was oriented at an angle of 30° with respect to the incoming laser beam, which irradiated the foil target at normal incidence. Using this geometry, the penumbral blurring due to the finite extent of the x-ray source is of the order of 0.2 μm.

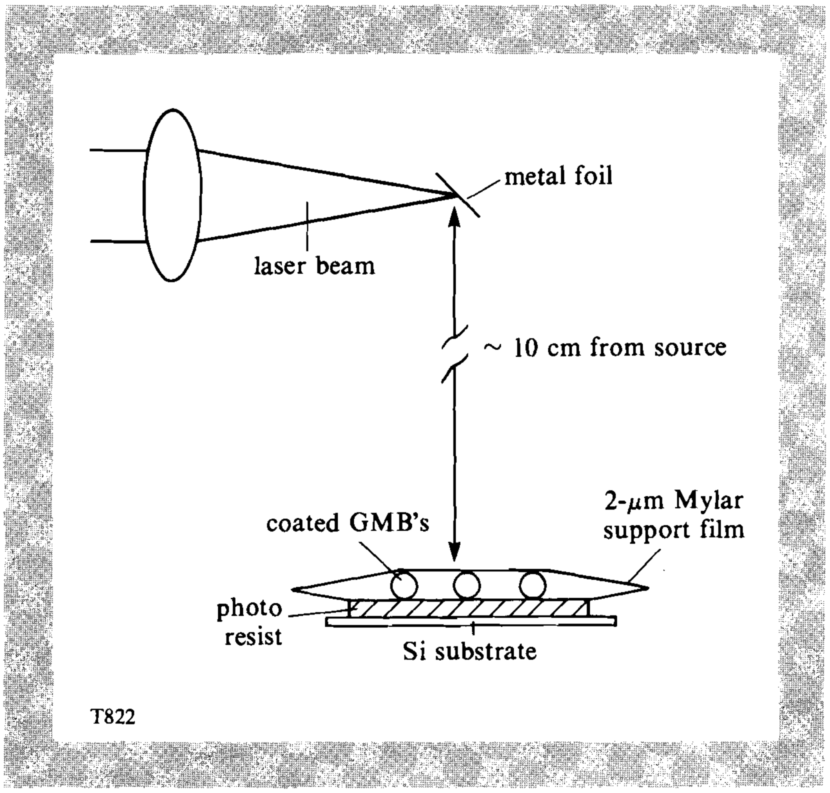

Fig. 30.2
Experimental configuration of x-ray microscopy, using a laser-produced plasma as an x-ray source.

Various target materials were tested in order to obtain the x-ray spectral characteristics and intensity required to produce useful images. X-ray emissions from silver, gold, copper, iron, and titanium foils irradiated by a single, 534-nm laser shot with an energy of 120 J were not energetic enough to produce significant image contrast between the CH coating and the underlying glass microshell. On the other hand, single laser shots with the same energy characteristics on molybdenum foils did produce x rays with the necessary spectral properties to make the plastic-glass interface quite visible. Multiple laser shots on molybdenum foils with the same photoresist sample remaining in the imaging assembly enabled a greater degree of x-ray exposure and created a clearly visible image of the plastic-glass interface with good contrast.

Upon exposure, the photoresist samples were developed as follows. The PBS-coated silicon wafer was held in a rapidly flowing stream of developer consisting of a 70% methyl isoamyl ketone/30% 2-pentanone mixture for 5 seconds. The wafer was then dipped in a 60% methyl isoamyl ketone/40% isopropyl alcohol rinse for 20 seconds. Compressed dry nitrogen was blown on the sample until the liquids were completely removed. The image present on the surface of the resist was then examined under a differential interference contrast microscope. The above development process was repeated until the desired contrast at the plastic-glass interface and the overall background-to-image contrast were obtained. Typical total times that the resist spent in the developer ranged from 5 to 25 seconds. Finally, to greatly increase the contrast of the resultant image, the photoresist film was postbaked for 30 min at 120°C. As stated by the manufacturer, the total linewidth variation resulting from the development procedure given above should be approximately 0.1 μm.

Results and Discussion

Several types of representative IF targets were used to evaluate this characterization technique. To examine the feasibility of the x-ray microscopy process in determining CH-coating parameters, glass microballoons and solid glass spheres with several-microns-thick plastic coatings were used. Also, in an effort to evaluate the ultimate resolution of this technique, batches of identical, precharacterized glass microballoons were coated with 0.4 to 1.0 μm of parylene in thickness increments of 0.2 ± 0.05 μm. These IF targets were then simultaneously evaluated using the x-ray microscopy technique with a laser-produced plasma. For comparison purposes, x-ray microscopy of the same targets was also performed using a conventional x-ray source producing 15-kV_{peak} bremsstrahlung at a source current of 2.5 mA. Using the conventional source under the same geometrical conditions as previously stated, exposures of two to four days were required to produce images of similar clarity.

Figure 30.3 shows an image typical of those produced, using the technique described in this report. This image was one of several made to determine if the necessary contrast could be obtained at the plastic glass interface and between the subject and background, and thus prove the feasibility of this technique. It was produced under the previously described laser and geometric conditions by two successive laser shots of nearly equal energy, which totaled 265 J on a molybdenum foil. Clearly visible is the 6-μm-thick CH coating on the

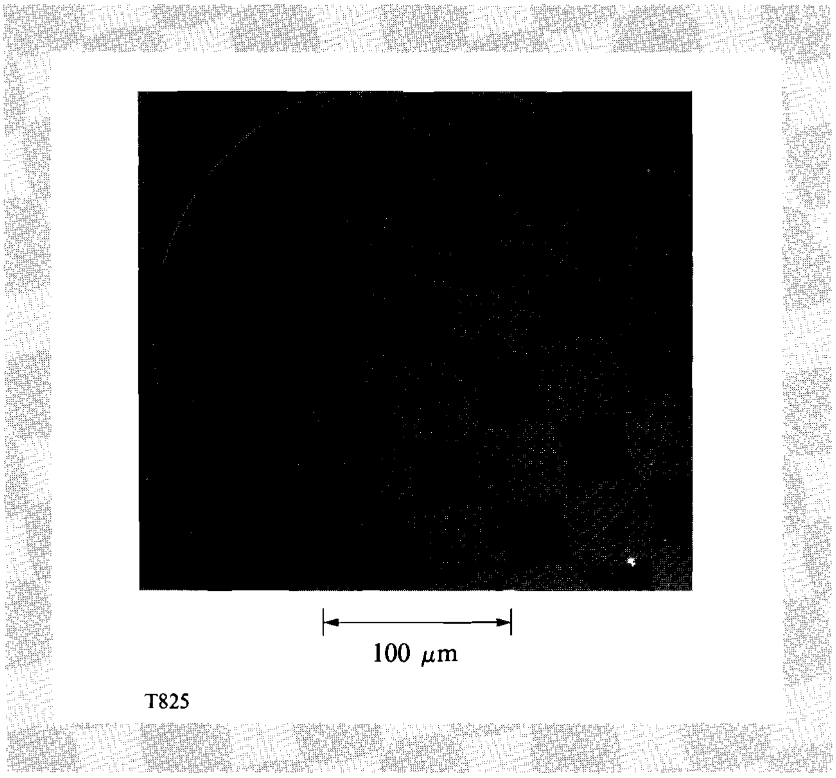

Fig. 30.3
X-ray micrograph of a glass microballoon coated with a 6-μm-thick parylene layer.

solid glass sphere. The variation in contrast about the perimeter of the image is a function of the optics used to view it and should be disregarded.

Figures 30.4(a) and 30.4(b) are included for image-quality comparison. In each, the outer rim of an image of the same IF target is shown. The image in Fig. 30.4(a) was made using the same laser-produced plasma as the image in Fig. 30.3. On the other hand, the one shown in Fig.30.4(b) was made using a conventional x-ray source under the conditions stated earlier. The laser-produced plasma emits x rays that do not have sufficient energy to appreciably pass through the glass shell; hence, only the 0.6-μm CH coating on its surface is visible in Fig. 30.4(a). On the other hand, the image in Fig. 30.4(b), produced using 15-kV_{peak} bremsstrahlung, clearly shows the 2-μm wall of the glass shell and, to a lesser extent, the outer CH coating. X rays in this energy range are not only sufficiently energetic to penetrate the glass microballoon, but they are capable of producing reasonable contrast between the glass and plastic layers.

In Fig. 30.4(a), there are no distinct lines delineating the plastic-glass and image-background interfaces. Instead, these regions are bordered by a brighter ring of finite width. This is chiefly caused by penumbral blurring because of the finite extent of the source, and the ultimate resolution of the microscope optics used to view and enlarge it.

Penumbral blurring of the image can be reduced by increasing the distance from the source to the sample; however, penumbral blurring decreases linearly with increased distance, while the x-ray irradiance on the imaging medium falls off quadratically. Hence, exposure is sacrificed as the penumbral blurring is reduced. The spatial resolution

Fig. 30.4
(a) X-ray micrograph of a glass microballoon overcoated with a 0.6-μm-thick parylene layer.
(b) X-ray micrograph of the same IF target but using a conventional bremsstrahlung source.

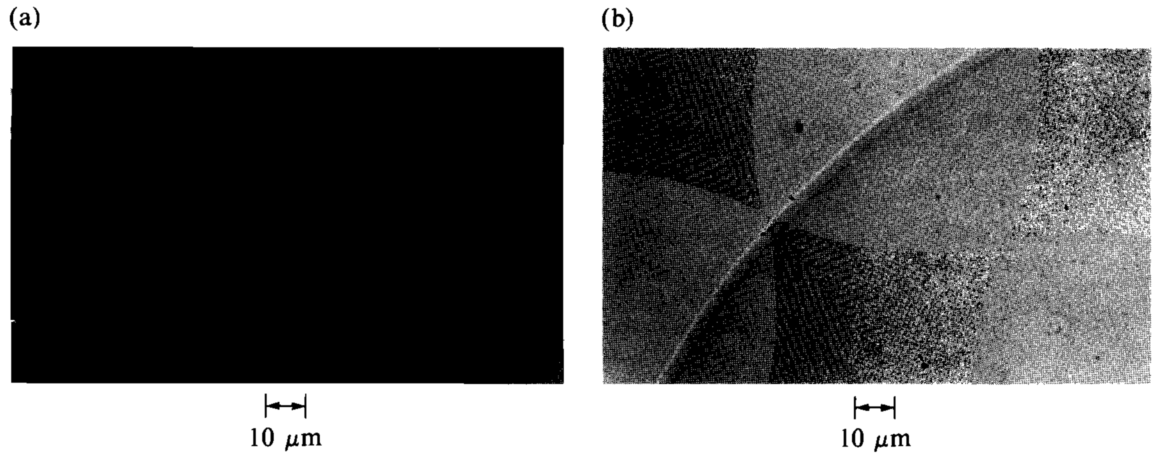

T826

can be improved by using scanning electron microscopy to view the resultant image; but, because PBS was designed to be an electron beam resist, damage to the image occurs immediately upon examination. Certain replication techniques and subsequent viewing with a transmission electron microscope have been developed to alleviate this problem.[14]

A comparison can be made between the images shown in Figs. 30.4(a) and 30.5 to determine experimentally the ultimate resolution of this technique under the present geometrical conditions. In Fig. 30.4(a), the 0.6-μm CH coating is comprised of two 0.2-μm blurred rings as described above, with a 0.2-μm gap between them. The outer blurred ring corresponds to the outer edge of the target and the inner blurred ring to the CH-glass interface. However, this gap is not seen in the image of the 0.4-μm coating shown in Fig. 30.5: the blurred interfaces between the glass and plastic and between the image and background have merged and, therefore, the limit of the resolution is of the order of half this coating thickness, i.e., ~0.2 μm. This number is in agreement with the penumbral blurring as calculated from the previously stated geometric conditions; it is also of the order of the resolution limit of an optical microscope. Therefore, using this technique under the present conditions, material coating thicknesses under 0.4 μm cannot be determined.

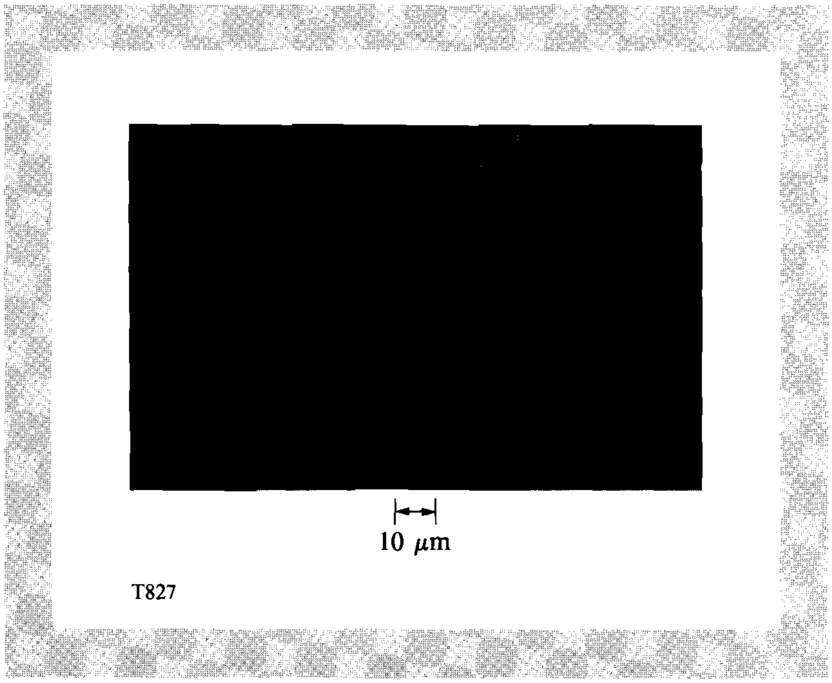

Fig. 30.5
X-ray micrograph of a glass microballoon overcoated with a 0.4-μm-thick parylene layer.

Conclusions

We have developed a soft x-ray contact microscopy technique to characterize submicron CH coatings on IF targets with a resolution of ~0.2 μm. The process is a hybrid of soft x-ray contact microradiography and x-ray lithography, and uses a laser-produced plasma as an x-ray source. When time is not a constraint, the process can be performed in the laboratory with a conventional stationary target x-ray source to yield similar results. The most significant advantage of this technique over microradiography is that it enables submicron resolution of CH coating layers without the need for costly and time-consuming digital image analysis.

ACKNOWLEDGMENT

This work was supported by the U.S. Department of Energy Office of Inertial Fusion under agreement No. DE-FC08-85DP40200, and by the Laser Fusion Feasibility Project at the Laboratory for Laser Energetics, which has the following sponsors: Empire State Electric Energy Research Corporation, General Electric Company, New York State Energy Research and Development Authority, Ontario Hydro, and the University of Rochester. Such support does not imply endorsement of the content by any of the above parties.

REFERENCES

1. B. A. Brinker, J. M. Cavese, J. R. Miller, S. G. Noyes, S. Sheble, and L. T. Whitaker, *J. Vac. Sci. Technol. A* **1**, 941 (1983).
2. R. Q. Gram, H. Kim, J. F. Mason, and M. Wittman, *J. Vac. Sci. Technol. A* **4**, 1145 (1981).
3. H. Kim and M. D. Wittman, *J. Vac. Sci. Technol. A* **3**, 1262 (1985).
4. T. M. Henderson, D. E. Cielaszyk, and R. J. Simms, *Rev. Sci. Instrum.* **48**, 835 (1977); R. L. Whitman and R. H. Day, *Appl. Opt.* **19**, 1718 (1980); R. M. Singleton and J. T. Weir, *J. Vac. Sci. Technol. A* **18**, 1264 (1981).
5. R. M. Day *et al.*, 8th International Congress on X-Ray Optics and Microanalysis (1977), pp. 260–267.
6. R. Feder and D. Sayre, *Ann. NY Acad. Sci.* **342**, 213 (1980).
7. E. Spiller, R. Feder, and J. Topalian, *Phys. Technol.* **22** (January 1977).
8. P. C. Cheng, J. Wm. McGowan, K. H. Tan, R. Feder, and D. M. Shinozaki, in *Examining the Submicron World*, edited by R. Feder *et al.* (Plenum, New York, 1986).
9. R. Feder *et al.*, *Science* **197**, 259 (1977); K. H. Tan, P. C. Cheng, G. M. Bancroft, and J. Wm. McGowan, *Can. J. Spectrosc.* **29**, 134 (1984).
10. J. Bailey, Y. Ettinger, A. Fisher, and R. Feder, *Appl. Phys. Lett.* **40**, 33 (1982); R. Feder, J. S. Pearlman, J. C. Riordan, and J. L. Costa, *J. Microsc.* **135**, 347 (1984).
11. M. L. Gimer, in *X-Ray Microscopy*, edited by G. Schmahl and D. Rudolph (Springer-Verlag, 1984); P. Gohil *et al.*, *Appl. Opt.* **24**, 2024 (1985).
12. B. Yaakobi, H. Kim, J. M. Soures, H. W. Deckman, and J. Dunsmuir, *Appl. Phys. Lett.* **43**, 686 (1983).
13. Mead Technologies, Inc., Rolla, MO.
14. P. C. Cheng *et al.*, *Nuclear Instruments and Methods in Physics Research* **A246**, 668–674 (1986).

1.B Improvements in the Coefficient for Inverse Bremsstrahlung Laser Absorption

Introduction

The classical coefficient for inverse bremsstrahlung (ib) laser absorption is proportional to a logarithmic factor, $\ln\Lambda_{ib}$, characteristic of Coulomb collisions. The argument Λ_{ib} generally is not calculated exactly but rather is estimated from physical considerations.[1] For low-density plasmas ($<10^{20}\text{cm}^{-3}$), $\ln\Lambda_{ib}$ is sufficiently large (>10) that the error in estimating Λ_{ib} should produce less than a ~10% variation in the logarithm, which is acceptable for most calculations. However, at the high plasma densities characteristic of short-wavelength laser irradiation (e.g., $\sim 9 \times 10^{21}$ cm^{-3} for 0.35-μm light), $\ln\Lambda_{ib}$ is <5, and uncertainties in $\ln\Lambda_{ib}$ can produce a 20% to 50% modification in the absorption coefficient. A more exact treatment of this term is presented here for the quantum-mechanical and classical limits of $\ln\Lambda_{ib}$, corresponding to low-Z and high-Z plasmas respectively.

For low-Z plasmas, a modified Born approximation is used to treat the electron-photon and electron-ion (e-i) interactions. The new features of the calculation are: (1) the time-dependent response of the plasma is modeled by including the plasma dielectric function as part of the Born-approximation treatment of the e-i interaction, and (2) an explicit treatment of ion-ion correlations replaces the usual assumption that the electrons scatter in an average electrostatic potential determined by the average positions of neighboring ions (e.g., a Debye-Hückel potential). This approach recovers the frequency dependence of $\ln\Lambda_{ib}$ obtained by Dawson and Oberman,[2] but it does not contain their indeterminate quantity k_{max}, which results from close e-i collisions. Close collisions are well described by the Born approximation in terms of the electron deBroglie wavelength.

The Born-approximation calculation is valid only for low-Z materials. For Z greater than ~10, any quantum mechanical treatment must include nonlinearities due to strong distortion of the electron wave function by the central ion, and in general a partial wave calculation is used. However, for the region of density and temperature of interest for laser absorption, the minimum-impact parameter for e-i collisions at high Z is no longer characterized by the deBroglie wavelength but by the classical-impact parameter for 90° scattering; thus, a quantum mechanical treatment is not required. The Coulomb logarithm could, in fact, be calculated using the classical nonlinear electron trajectory; that is the approach taken here for moderate-Z and high-Z plasmas. First, the logarithmic term for e-i scattering, $\ln\Lambda_{ei}$, is calculated for an average potential; then, a correction term (obtained from the Born approximation) is added to obtain the Coulomb logarithm for inverse bremsstrahlung, $\ln\Lambda_{ib}$. The Coulomb logarithm for e-i scattering ($\ln\Lambda_{ei}$) in a Debye-Hückel potential has been previously calculated over the quantum-mechanical and classical regions with the approximation $\Lambda_{ei} >> 1$, appropriate for moderate-Z ions ($Z < 25$). We extend those calculations to the high-Z region by including the effects of strong ion-ion correlations described by a nonlinear Debye-Hückel model, which merges smoothly with the previous large-Λ results. The electron trajectory in the resulting electrostatic potential is calculated numerically.

Physical Parameters and Definitions

Inverse bremsstrahlung is the process of light absorption induced by electron-ion collisions. The Coulomb logarithm generally is written in terms of the classical-impact parameters characterizing e-i scattering:

$$\ln\Lambda = \ln\,(b_{\max}/b_{\min}) + C \quad , \tag{1}$$

where $b_{\max}$ is the maximum impact parameter, $b_{\min}$ is the impact parameter for 90° scattering, and C is a number containing the remainder of the term, which is generally of the order of 1. For laser absorption, a correct calculation of $\ln\Lambda_{\mathrm{ei}}$ should include (1) the response of plasma electrons to laser light in the presence of electron-ion scattering; (2) plasma shielding of interacting charged particles; (3) ion-ion correlations; and (4) nonlinear orbit dynamics or quantum-mechanical wave effects for close collisions. Various approximations have been used to determine the parameters in Eq. (1); no single approximation has determined all parameters self-consistently over the entire range of interest. (Of course, $\ln\Lambda$ would be well defined in a complete quantum mechanical calculation.)

The classical plasma calculation[2] for laser absorption has determined $b_{\max}$ in terms of the plasma Debye length λ_D and the laser frequency ω. Physically, these parameters play the following role. In a plasma, each ion is shielded by neighboring electrons and ions; for a low-Z to moderate-Z, high-temperature plasma the characteristic screening length is the Debye length

$$\lambda_D = [4\pi n_e e^2\,(1/T_e + Z/T_i)]^{-1/2} \quad , \tag{2}$$

where n_e is the electron density, T_e the electron temperature, T_i the ion temperature, and Z the ionic charge. Typically, T_e can be two to three times larger than T_i, as the e-i equilibration time can be much longer than the electron-heating time by inverse bremsstrahlung. The results below use $T_e = T_i$ for simplification, but the modification of the shielding distance for unequal temperatures is straightforward. Often, only the electron contribution to shielding is used [i.e., $Z = 0$ in Eq. (2)], which is based on the approximation of a uniform, ion background. But more realistic models, which include ion-ion correlations, show that the ion contribution to shielding can be dominant, as discussed below. For impact parameters much larger than the shielding distance, e-i scattering (and hence inverse bremsstrahlung) is negligible. Besides shielding, an additional factor enters into the determination of $b_{\max}$: the electron collision time should not be much longer than the period of the electromagnetic wave; otherwise, the interaction would be almost adiabatic and very little energy would be transferred to the electrons. The interaction time for an electron with an impact parameter b is roughly b/v_t, where $v_t = (T_e/m)^{1/2}$. Combining these two factors, the maximum impact parameter is approximated by

$$b_{\max} = \min\,(\lambda_D,\ v_t/\omega)\quad , \tag{3a}$$

which is characteristic of the detailed classical result.[2] Often only the high-frequency limit (low density) of the plasma calculation is quoted,[1] i.e., $b_{\max} = v_t/\omega$. This is not valid near the critical density where a majority of the laser light is absorbed. In this region, λ_D more closely characterizes the maximum impact parameter; it is approximately a factor $(Z+1)^{1/2}$ smaller than v_t/ω.

The choice of λ_D as the shielding length is only valid when it is much larger than the average-ion radius R_o, defined as $(4\pi n_i/3)^{-1/3}$. For high-Z plasmas, λ_D can become smaller than R_o, and strong ion-ion correlations must be considered for evaluating the plasma shielding. In this case, often the larger of R_o and λ_D is used.[3,4] This condition will be denoted here by an asterisk, i.e.,

$$b^*_{\max} = \min\,[\max(\lambda_D, R_o),\ v_t/\omega]\quad . \tag{3b}$$

The minimum impact parameter $b_{\min}$ in Eq. (1) is left indeterminate in the classical-plasma calculation.[2] It is often approximated by the impact parameter b_{90} for 90° scattering of an electron in a Coulomb potential,

$$b_{90} = Ze^2/mv^2\quad , \tag{4}$$

where v is the electron velocity. If b_{90} is smaller than approximately the deBroglie wavelength, then quantum-mechanical effects must be considered. Typically, the quantum-mechanical "minimum-impact parameter" is defined as[5]

$$\lambda_q = \hbar/2mv\quad . \tag{5}$$

The parameter $b_{\min}$ becomes

$$b_{\min} = \max\,(b_{90},\ \lambda_q)\quad , \tag{6}$$

and is evaluated here at the effective velocity given by the energy relation

$$\frac{1}{2}mv^2 = \frac{3}{2}T\quad . \tag{7}$$

The region where $b_{\min} = \lambda_q$ will be denoted here as quantum mechanical, and the remaining region, will be called classical.

It is convenient to define a standard Coulomb logarithm, $\ln\Lambda_s$ to compare with the new results discussed below. We use

$$\ln\Lambda_s = \ln(b_{\max}/b_{\min})\quad , \tag{8}$$

with Eqs. (3) and (6) defining the impact parameters, and with C from Eq. (1) set equal to zero. We denote the classical and quantum-mechanical limits of Λ_s as Λ_c and Λ_q respectively. The classical limit of Eq.(8) is

$$\ln\Lambda_c = \ln(12\,\pi n_e\,\lambda^3_D)\quad , \tag{9a}$$

which has been evaluated near the critical density n_c with $\lambda_D < v_t/\omega$ and with the approximation $Z \approx Z + 1$. For high density, Λ_c is modified by Eq. (3b), in which the average-ion radius is used as the shielding distance

$$\Lambda_c^* = \Lambda_c \cdot \max(1, R_o / \lambda_D) \quad . \tag{9b}$$

In the quantum mechanical limit, Eq. (8) becomes

$$\ln\Lambda_q = \ln(\sqrt{12\, mT} / \hbar k_D) \quad , \tag{10}$$

where $k_D = 1/\lambda_D$.

Boundaries characterizing the different regions are sketched in Fig. 30.6, for Z versus T, at a plasma electron density of 9×10^{21} cm^{-3}. Temperatures around 1 keV are typical of laser-irradiated plasmas. The boundary between the quantum-mechanical and classical regions is determined by the condition $b_{90} = \lambda_q$. Except for the lowest-Z materials, lnΛ is in the classical region and can be determined by classical-orbit dynamics. Even for CH ($Z \sim 3$) at $T < 1$ keV, lnΛ is nearly classical. For moderate-Z and high-Z materials, Fig. 30.6 shows that approximations based on a linearized Debye-Hückel model may not be adequate, as $\lambda_D < R_o$. At high Z, approximations based on $\Lambda >> 1$ are questionable.

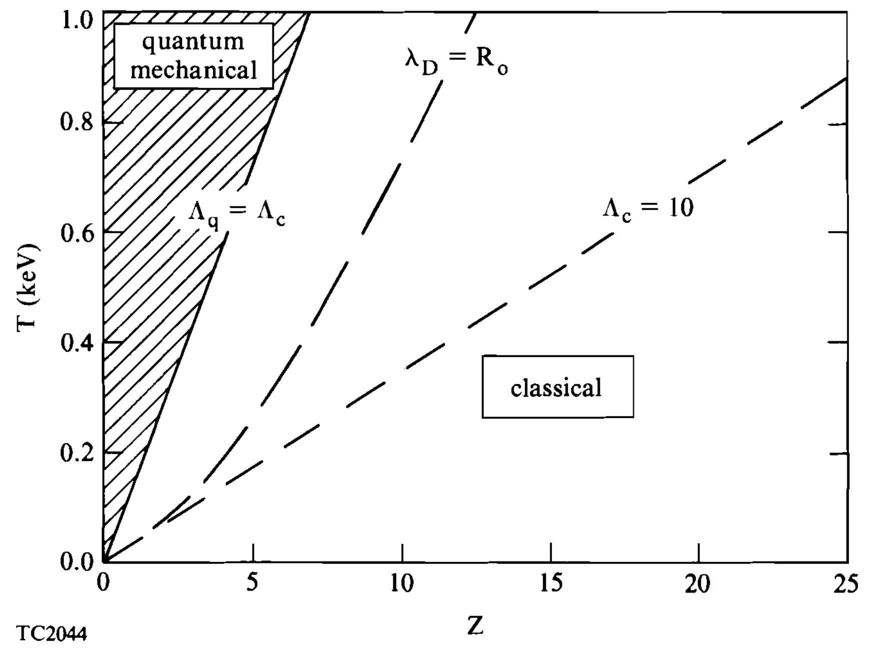

Fig. 30.6

Different regions and parameters characterizing $\ln\Lambda \sim \ln(b_{\max}/b_{\min})$. In the shaded region, the deBroglie wavelength, Eq. (5) determines $b_{\min}$; in the remainder b_{90}, Eq. (4), is the appropriate minimum impact parameter. For Z greater than ~ 25, the Debye length λ_D, Eq. (2) becomes comparable to the average-ion radius R_o and strong ion correlations become important in determining $b_{\max}$; approximations based on $\Lambda >> 1$ may become inaccurate.

Although the quantum-mechanical region (low Z) is relatively small, it is of considerable importance because low-Z ablators are required for direct-drive laser fusion. In this region, an accurate expression for $\ln\Lambda$ can be obtained relatively simply by using the Born approximation. This approximation is applicable[6] when the kinetic energy of the interacting electrons is much larger than the potential energy at approximately a deBroglie wavelength from the ion, i.e., $1/2\ mv^2 > Ze^2/(\hbar/mv)$, or, using Eqs. (5) and (7):

$$T > 35\ Z^2\ \mathrm{eV} \quad , \tag{11}$$

corresponding to a low-Z, high-temperature plasma. (This condition is equivalent to $b_{90} > \lambda_q$.) As discussed later in **Results**, the Born approximation determines all parameters in the interaction: the classical result for $b_{\max}$ is recovered in the Born approximation when the Coulomb potential is modified by the plasma dielectric function; $b_{\min}$ is obtained in terms of the deBroglie wavelength; and $C \sim -1$. Results similar to these were obtained by Cauble and Rozmus[7], who used a modified Coulomb potential that phenomenologically accounted for quantum-wave effects in close electron-ion collisions.

The Born-approximation model is applicable to laser absorption for CH ($Z \sim 3$), but is invalid for SiO_2 ($Z = 10$) and for higher-Z materials at keV temperatures characteristic of laser-plasma interactions. We extend the calculation of $\ln\Lambda$ into the higher-Z region by relating the inverse-bremsstrahlung Coulomb logarithm $\ln\Lambda_{\mathrm{ib}}$ to the logarithm for electron-ion scattering, $\ln\Lambda_{\mathrm{ei}}$, in a shielded electrostatic potential. The Born approximation shows this relation to be

$$\ln\Lambda_{\mathrm{ib}}(\mathrm{Born}) = \ln\Lambda_{\mathrm{ei}}\ (\mathrm{Born}) + \frac{1}{2} + \frac{1}{Z}\, O\,(1/2) \tag{12}$$

near the critical density. The term 1/2 is the result of averaging $\ln\Lambda_{\mathrm{ib}}$ over all ion positions, compared to simply using an average electrostatic potential (Debye-Hückel) in the calculation of $\ln\Lambda_{\mathrm{ei}}$, as discussed by Hubbard and Lampe.[8] Equation (12) is extrapolated into the high-Z region, beyond the validity of the Born approximation, according to

$$\ln\Lambda_{\mathrm{ib}} = \ln\Lambda_{\mathrm{ei}} + [\ln\Lambda_{\mathrm{ib}}(\mathrm{Born}) - \ln\Lambda_{\mathrm{ei}}\ (\mathrm{Born})] \quad , \tag{13}$$

which is similar to Eq. (7) in Ref. 9. This extrapolation is probably the largest source of uncertainty for high Z. The term 1/2 makes a 25% contribution to $\ln\Lambda_{\mathrm{ib}}$ for $Z = 50$. Using Eq. (13), $\ln\Lambda_{\mathrm{ib}}$ can be determined by calculating e-i scattering in a spherically symmetric potential. An expression for $\ln\Lambda_{\mathrm{ei}}$ that spans the quantum-mechanical and classical limits has been obtained by Williams and DeWitt,[9] for moderate Z. However, their results depend on the approximate solution by Liboff[10] for electrons scattering in a linearized Debye-shielded potential with $\Lambda \gg 1$, and is not appropriate for high-Z plasmas.

For high-Z materials with Λ less than ~ 10, the potential around an ion can no longer be described by the linearized Debye-Hückel model, and stronger ion-ion correlations must be considered. Such correlations were examined by Cauble and Rozmus,[7] but with a model that produces only the quantum-mechanical minimum-impact parameter. This is valid only at low Z, where the strong ion correlations occur at very low temperatures; these conditions are not characteristic of the laser absorption region. In this article, strong ion-correlation effects are examined at the higher temperatures achieved in coronal high-Z plasmas. A nonlinear Debye-Hückel (NLDH) model[11,12] is used to prevent the close approach of neighboring ions, which is the main effect of strong correlations. The Coulomb logarithm is evaluated by using the classical electron trajectory in the NLDH self-consistent electrostatic potential. This model is convenient for considering electrons and ions at different temperatures, and it merges smoothly with the low-Z (large-Λ) results of Liboff for a linearized Debye-shielded potential.

The starting point for the calculation is Boltzmann's equation for the change in the electron distribution function f due to inverse bremsstrahlung:

$$\frac{\partial f}{\partial t} - \frac{e}{m} E \cdot \nabla_v f = \int d^3\Delta v$$

$$\times \left[W(v-\Delta v \Rightarrow v)\, f(v-\Delta v) - W(v \Rightarrow v+\Delta v)\, f(v) \right] \quad . \qquad (14)$$

The electric field E and the two-body interaction W can take on different meanings according to the particular model of the laser-plasma interaction. Three models are considered:

(a) The first model, by Dawson and Oberman[2], treated all e-i scattering as a self-consistent electrostatic potential, which was included in E together with the laser electric field. Close two-body interactions were considered negligible, and the term W was set equal to zero. This approach is able to calculate the collective plasma effects but not the close e-i encounters, which are reflected by an indeterminate quantity $k_{\max}$ in the effective Coulomb logarithm.

(b) A second approach, based on the Born approximation, places both the laser electric field and e-i collisions into the term W, in terms of an inverse-bremsstrahlung transition rate, and E is set equal to zero. Close e-i collisions are now treated accurately (within the range of validity of the Born approximation), and the collective plasma effects of (a) are recovered by using the plasma dielectric function to modify the vacuum Coulomb potential around an ion. There are no indeterminate parameters in this model,[13] but its validity is limited to very low ionic charge.

(c) The third model assumes that electron oscillation in the laser electric field does not modify e-i scattering and can be separated from it: the laser electric field is included in E, and e-i scattering (in an electrostatic potential) is in the term W. This model is used for high-Z plasmas.

Results

1. Low *Z*

Two features characterize the Coulomb logarithm for laser absorption in low-Z materials: (1) the plasma shielding distance λ_D is sufficiently large that the ω/v_t contribution to b_{max} can introduce an ω dependence to Λ [Eq. (3a)]; and (2) the impact parameter for 90° electron scattering is sufficiently small that quantum-wave effects can contribute to b_{min} [Eq. (6)]. The first effect has been calculated by Dawson and Oberman.[2] Both effects are simultaneously addressed by the Born approximation result. (A schematic of the processes considered in the Born approximation is shown in Fig. 30.7.) Using the Born approximation, with a Coulomb potential modified by the plasma dielectric function, we obtain

$$\begin{aligned}\ln \Lambda_{ib}\,(\text{Born}) = {} & \ln\Lambda_q + \ln[(Z+1)^{1/2}/\bar{\omega}] - \gamma + \frac{1}{2}\ln(4/3) \\ & + \frac{1}{2\,Z}\, e^{\bar{\omega}^2/2}\, E_1(\bar{\omega}^2/2) \\ & - \frac{Z+1}{2\,Z}\, e^{\bar{\omega}^2/2(Z+1)}\, E_1[\bar{\omega}^2/2(Z+1)] \ , \qquad (15)\end{aligned}$$

where $\ln\Lambda_q$ is the standard quantum-mechanical Coulomb logarithm defined in Eq. (9), γ is Euler's constant (γ = 0.577), E_1 is the exponential integral, and $\bar{\omega} = \omega/\omega_p$ (where ω_p is the local plasma frequency; or, in terms of the critical density, $\bar{\omega}^2 = n_c/n$). To compare the Born-approximation result with Dawson and Oberman,[2,14] we examine the two limits: (1) absorption near the critical density [$\bar{\omega} \sim 1$ in Eq. (15)], and (2) absorption at very low density ($\bar{\omega} >> 1$). It is the latter limit that is most often quoted,[1] but it is the former that is most relevant to laser-fusion experiments.

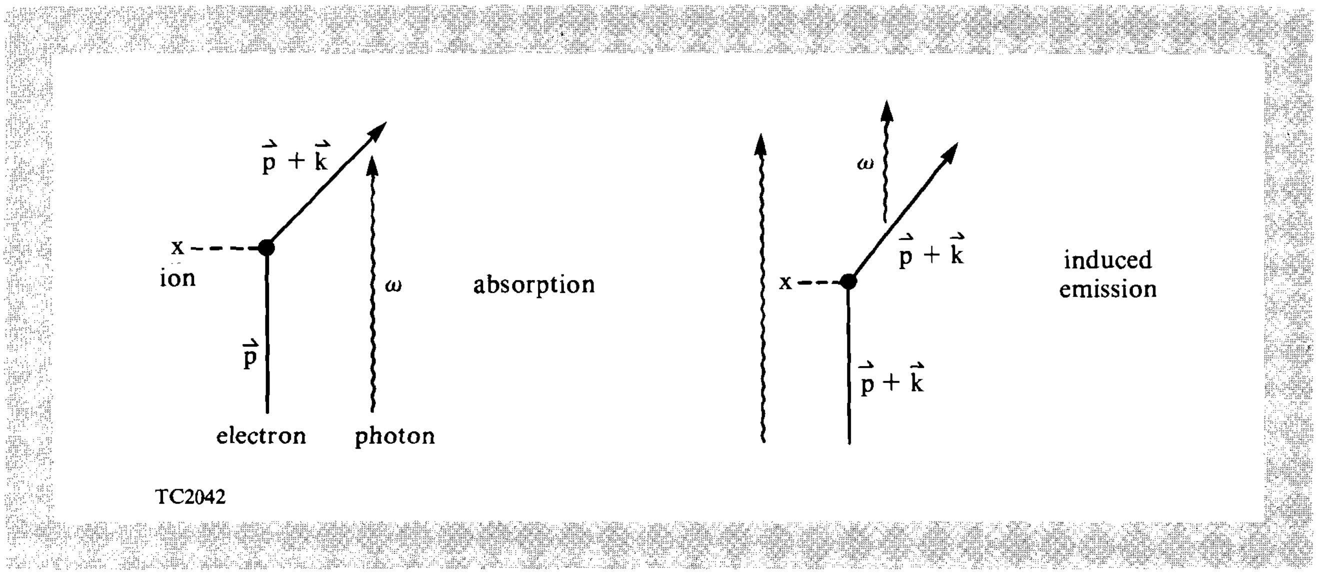

Fig.30.7
Schematic of the processes contributing to inverse bremsstrahlung in the Born approximation. Momentum transfer by the photon is neglected.

In the high-frequency limit ($\bar{\omega} >> 1$) appropriate for low-density absorption, both exponential integrals in Eq. (15) approach zero, leaving

$$\ln \Lambda_{\mathrm{ib}} \approx \ln(4\ T/\hbar\omega) - \gamma \ . \tag{16}$$

(The same result has been obtained for bremsstrahlung emission[15] in the Born approximation with $\hbar\omega << T$, for a pure Coulomb potential.) To compare with the Dawson-Oberman result $\ln\Lambda_{\mathrm{DO}}$ the indeterminate quantity k_{max} ($= 1/b_{\mathrm{min}}$) in Ref. 2 is replaced by the suggested quantum mechanical expression, $k_{\mathrm{max}} = (mT)^{1/2} / \hbar$. The difference from Eq. (16) is found to be $\ln\Lambda_{\mathrm{ib}} - \ln\Lambda_{\mathrm{DO}} \approx 0.75$, representing a 15% correction for conditions attained in short-wavelength laser irradiation of CH, characterized by $\ln\Lambda \approx 5$.

For the region around the critical density ($\bar{\omega} \sim 1$), Eq. (15) reduces to

$$\ln \Lambda_{\mathrm{ib}} \approx \ln\Lambda_q + \frac{1}{2}\ln(2/3) - \frac{1}{2}\gamma - \frac{1}{2Z}\ln(Z+1) \ , \tag{17}$$

where we have also assumed $Z^{1/2} / \bar{\omega} >> 1$. This should be compared with the $\omega << \omega_p$ case of Dawson in Ref. 14, $\ln\Lambda_{\mathrm{D}}$, evaluated at $\omega = \omega_p$. (When the effects of ion shielding are included, the results for large and small ω are no longer equal at $\omega = \omega_p$ as they were in Ref. 1, which used only electron shielding. The $\omega << \omega_p$ result is the one that best approximates the correct solution for $\omega = \omega_p$.) Again, the suggested replacement $k_{\mathrm{max}} = (mT)^{1/2} / \hbar$ was used, with the same result for the difference in solutions: $\ln\Lambda_{\mathrm{ib}} - \ln\Lambda_{\mathrm{D}} \approx 0.75$. In the region that dominates laser absorption, the ω dependence of $\ln\Lambda_{\mathrm{ib}}$ is found to be negligible.

Equation (17) is similar to the result obtained by Cauble and Rozmus[7], who did not use the Born approximation but rather a modified Coulomb potential that approximates quantum effects at small distances. Their resulting Coulomb logarithm differs from the one here by only ~0.1 for $Z = 3$. Cauble and Rozmus note that there is a substantial difference between their results (with linear, Debye-Hückel ion correlations) and the Dawson-Oberman results from Ref. 2, which indeed did not include the ion contribution to shielding. However, if comparison had been made with Ref. 14 instead, where Dawson has removed the assumption of a random ion distribution and imposed Debye-Hückel correlations, then very little difference would have been found (using the $\omega << \omega_p$ result for the region around the critical density). The remaining difference could be removed by modifying the choice of k_{max}, which does not depend on ion correlations.

The relationship between $\ln\Lambda_{\mathrm{ib}}$ and the classical high- and low-frequency limits is shown in Fig. 30.8, over the density range from 0.1 n_c to n_c, for a 1-keV plasma with $n_c = 9\times10^{21}$ cm^{-3}. Although $\ln\Lambda_{\mathrm{DO}}(\omega << \omega_p)$ was derived for $n > n_c$, it is evaluated here at the subcritical density indicated. Over this density range, where laser absorption predominantly occurs, $\ln\Lambda_{\mathrm{ib}}$ is well approximated by the

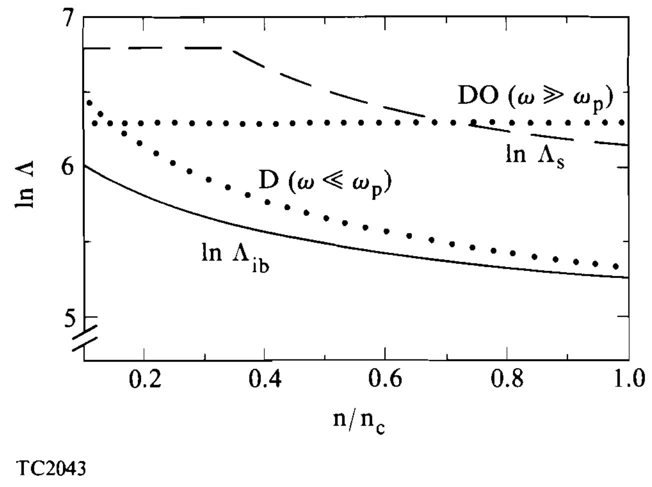

Fig. 30.8
The density dependence of $\ln\Lambda_{ib}$ (Born) for $Z = 3$, $T = 1$ keV in terms of the critical density n_c (9×10^{21} cm^{-3}). Compared are Eq. (8) for $\ln\Lambda_s$, the Dawson and Oberman (DO) result[2] for $\omega >> \omega_p$, and Dawson's (D) result[15] derived for $\omega << \omega_p$ but evaluated at the $\omega > \omega_p$ density indicated. Over the region shown, $\ln\Lambda_{ib}$ is best approximated by the $\omega << \omega_p$ result. Only at densities below $\sim 0.1\ n_c$ does $\ln\Lambda_{ib}$ reach the $\omega >> \omega_p$ result.

$\omega << \omega_p$ result. Only at densities well below 0.1 n_c does $\ln\Lambda_{ib}$ approach the high-frequency limit. Use of the high-frequency limit around n_c results in a $\sim$20% error for low Z.

2. High Z

For high Z, where Λ is less than ~ 10, we use Eq. (13) to calculate $\ln\Lambda_{ib}$ from e-i scattering in an average, self-consistent, electrostatic potential. In this region, corresponding roughly to $Z > 25$, Fig. 30.6 shows that it would be questionable to use λ_D as the shielding distance, or to use approximations dependent on $\Lambda >> 1$. Here we evaluate $\ln\Lambda_{ei}$ by numerically calculating the electron trajectory in the nonlinear Debye-Hückel potential to determine the relationship between the impact parameter b and the scattering angle θ. The relation between the scattering cross section σ and the Coulomb logarithm for e-i scattering is given by

$$\ln \Lambda_{ei} = \frac{1}{8}\int dv\; v\, f_o(v) \int_{-1}^{1} \bar{\sigma}(\theta,v)\, (1-\cos\theta)\, d\cos\theta \;/\; \int f_o\; v\; dv \quad . \tag{18}$$

The dimensionless quantity $\bar{\sigma}$ is defined as

$$\bar{\sigma} = \sigma(\theta,v) \;/\; \sigma_c(180°,v) \quad , \tag{19}$$

in terms of $\sigma_c = (Ze^2/2\ mv^2)^2$, the cross section for 180° scattering in a pure Coulomb potential. The first velocity moment of the distribution function is required for inverse bremsstrahlung. (Other e-i processes such as electron diffusion would require higher-order moments.) Using $\sigma\ d\cos\theta = b\ db$, the double integral in Eq. (18) is calculated numerically, and finally, $\ln\Lambda_{ib}$ is evaluated from $\ln\Lambda_{ei}$ using Eq. (13).

The electrostatic potential $V(r)$ is calculated from Poisson's equation, without linearization:

$$\nabla^2 V = -4\,\pi e\,(Z\,n_i - n_e) \quad ; \tag{20}$$

$$n_e = Z\langle n_i\rangle \, \exp(eV/T_e) \quad ; \tag{21}$$

$$n_i = \langle n_i\rangle \, \exp(-eZV/T_i) \quad ; \tag{22}$$

with the boundary conditions $V(\infty) = 0$ and $V(r \Rightarrow 0) = Ze/r$. The Fermi-Dirac form of the electron distribution function was also used because n_e can become large (and degenerate) near the nucleus; however, the degeneracy effect on $\ln\Lambda$ was found to be insignificant for the conditions considered here. If Eqs. (20) through (22) are linearized in terms of V, the usual Debye-Hückel shielding length is obtained. However, linearization is not valid within the average ion-sphere radius R_o, where V becomes large. Near the central ion, Eq. (22) forces the ion density of neighboring ions to rapidly approach zero, and only electrons remain for shielding.

The classical trajectory for an electron scattering in an arbitrary potential $V(r)$ is given by[16]

$$\theta = \pi + 2 \int_o^{u_o} \left[1 - V\!\left(\frac{1}{u}\right)/E - (bu)^2\right]^{-\frac{1}{2}} b\,du \quad , \tag{23}$$

where θ is the scattering angle, β is the impact parameter, and u is the inverse radius between the electron and the ion. The upper limit to the integral is given by the zero of the square-root factor and corresponds to the distance of closest approach.

This NLDH model for the ions is valid for values of the ion-ion coupling parameter Γ $(= Z^2 e^2/R_o T)$ less than ~ 1. For $Z = 50$, $T = 0.5$ keV and $n_e = 9 \times 10^{21}$, we have $\Gamma = 6$, which suggests that NLDH may be only marginally applicable. To test the sensitivity of $\ln\Lambda_{\mathrm{ib}}$ to the model, an alternate potential was tried: the potential was determined assuming a uniform electron density, which does not permit neighboring ions inside R_o. (The NLDH model does permit a small amount of neighboring ions to penetrate R_o.) For $Z \sim 50$, there was less than about a 2% difference between the models for the calculation of $\ln\Lambda_{\mathrm{ei}}$, and both gave values about a factor of 2 higher than the linearized Debye-Hückel model result. (For low Z, the NLDH model reproduces the linearized results of Liboff to within a few percent, while the uniform electron model is $\sim$50% lower and would not be applicable in this region.) This suggests the applicability of using the NLDH model to calculate $\ln\Lambda_{\mathrm{ei}}$ over the entire classical region, at the conditions considered here.

To test the numerical procedure, comparison was made with the free-free Gaunt factor calculated by Lamoureux *et al.*[17] They performed a quantum-mechanical partial-wave calculation of bremsstrahlung emission, produced by 1-keV electrons in a Ce ($Z = 55$) plasma at an ion density of 8.6×10^{21} cm^{-3}. The Gaunt factor G is related to the Coulomb logarithm by $G = (\pi^{1/2}/3)\,\ln\Lambda$.

Lamoureux *et al.* observe that G is relatively insensitive to the shapes of potentials with roughly the same range, as above. Their effective $\ln\Lambda$ in the soft-photon limit is 1.2. The classical model used here is in close agreement, predicting 1.3 for the NLDH potential.

The NLDH results for $\ln\Lambda_{\mathrm{ib}}$, as a function of Z, are presented in Fig. 30.9 for T = 1 keV and in Fig. 30.10 for T = 0.5 keV (both are at the critical density 9×10^{21} cm^{-3} for 0.35-μm light). Also shown in the figures are (1) $\ln\Lambda_{\mathrm{ei}}$, from Liboff's calculations, corresponding to the moments in Eq. (18); (2) $\ln\Lambda_s$, defined in Eq. (9a), which uses

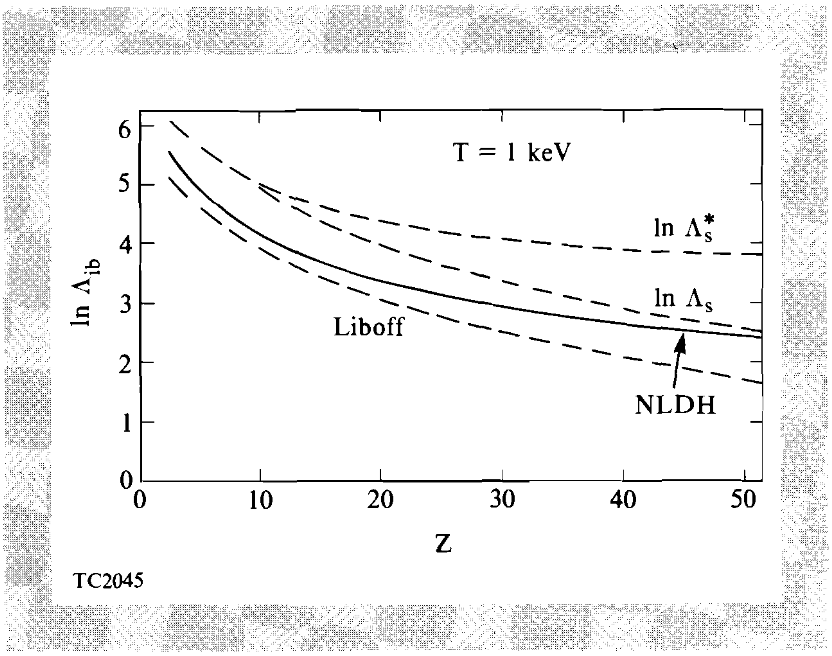

Fig. 30.9
$\ln\Lambda_{\mathrm{ib}}$, using nonlinear Debye-Hückel (NLDH) ion correlations, compared with the approximate $\ln\Lambda_{\mathrm{ei}}$ of Liboff,[10] $\ln\Lambda_s$ of Eq. (9a), which uses λ_{D} as the shielding length, and with $\ln\Lambda_s{}^*$, which uses the maximum of the ion-sphere radius R_o and λ_{D} as the shielding length. At higher Z (or lower temperature), both $\ln\Lambda_s$ and Liboff's result would become negative. The results are for $n_e = 9 \times 10^{21}$ cm^{-3} and T_e = 1 keV. Equation (24) is a good approximation to the NLDH results.

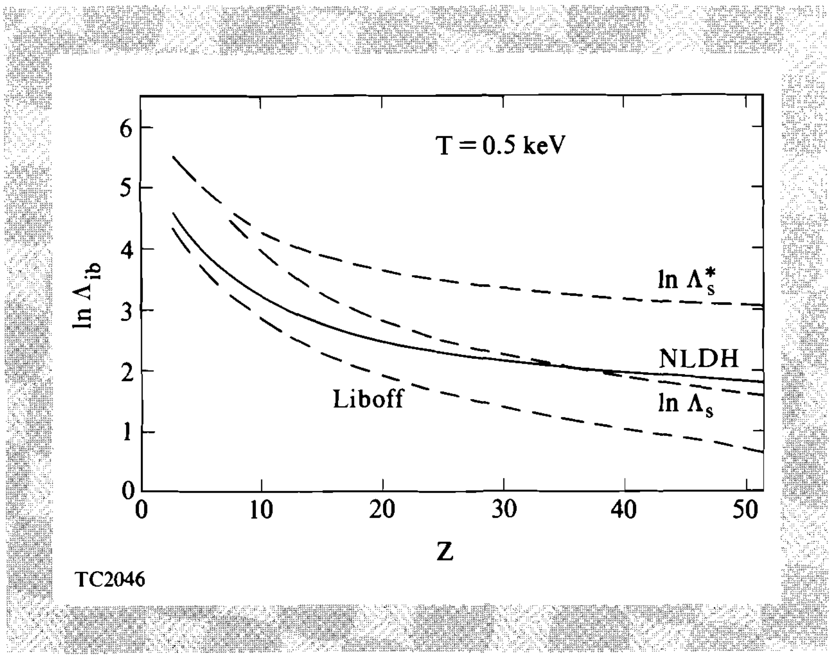

Fig. 30.10
Same as Fig. 30.9, but with T_e = 0.5 keV.

the Debye length λ_D as the shielding distance; and (3) $\ln\Lambda_s$*, which uses the average-ion radius as the shielding distance whenever it is larger than λ_D [Eq. (9b)]. We make the following observations: The deviation between $\ln\Lambda_s$ and $\ln\Lambda_s$* becomes apparent for Z greater than ~10, corresponding to the region of $R_o > \lambda_D$ in Fig. 30.6. Both $\ln\Lambda$ (Liboff) and $\ln\Lambda_s$ have the wrong functional form in this region, which would become negative at higher Z or lower T. Nevertheless, over the region shown, $\ln\Lambda_s$ is able to approximate the NLDH results to within ~10%.

The often-quoted high-frequency limit of Dawson and Oberman is not shown in the figures. Effectively, it uses only electron shielding for $b_{\max}$ and is related to $\ln\Lambda_s$ by

$$\ln\Lambda(\omega >> \omega_p) \approx \ln\Lambda_s + 1/2\ln_e(1+Z)-1.$$

For $Z = 50$, it would be in error by about 50% compared to $\ln\Lambda$(NLDH).

The NLDH solution decreases very slowly with Z, and does not fall much below 2. One result of the NLDH calculation is to support the use of $\max(R_o, \lambda_D)$ as the effective shielding distance. The $\ln\Lambda_s$* curve, which has this constraint, very closely follows the functional form of $\ln\Lambda$(NLDH) into the high-Z, low-temperature region. An approximation to $\ln\Lambda$(NLDH), to within a few percent, is

$$\ln\Lambda_{\mathrm{ib}}\,(\mathrm{NLDH}) = \ln\Lambda_s^* - 1.25 \tag{24}$$

for the conditions of temperature and density considered here, including the quantum-mechanical region. The nonlogarithmic term 1.25 contains all the details of the calculation. It corresponds to a ~50% effect at high Z.

For high Z, $\ln\Lambda_{\mathrm{ib}}$ is obtained by adding ~0.5 to $\ln\Lambda_{\mathrm{ei}}$ [Eqs. (12) and (13)]. This attempt to reduce the effect of different ion configurations to an average electrostatic potential represents a 25% variation for $Z \sim 50$. It is probably the greatest source of uncertainty in the calculation, and further investigation is needed.

Summary

The "Coulomb logarithm" for laser absorption has been calculated for conditions achieved in short-wavelength laser irradiation: $n_e \sim 10^{22}$ cm^{-3} and $T \sim 1$ keV. At these conditions $\ln\Lambda_{\mathrm{ib}}$ is < 5, and uncertainties in previously used models can produce variations in this term of 20% to 50%.

For low-Z materials, $\ln\Lambda_{\mathrm{ib}}$ was calculated quantum mechanically using a modified Born approximation. Collective plasma effects were included by multiplying the e-i interaction term by the plasma dielectric function. Unlike the classical calculation,[2] the "minimum impact parameter" was well determined and, of course, related to the deBroglie wavelength. The effective "maximum impact parameter" was the same as the classical result. The ω dependence of $\ln\Lambda_{\mathrm{ib}}$ was found to be negligible near the critical density n_c (Fig. 30.8), where absorption predominantly occurs. Use of the often-quoted high-frequency limit of $\ln\Lambda_{\mathrm{ib}}$ in this region can lead to a ~20% error. Near n_c, $\ln\Lambda_{\mathrm{ib}}$ is found to be closely related to $\ln\Lambda_{\mathrm{ei}}$, the Coulomb logarithm for electrons scattering in a shielded electrostatic potential around an ion; Eq. (13) was used to extrapolate that relationship beyond the range of validity of the Born approximation into the high-Z region.

For Z greater than ~10, the minimum impact parameter is no longer quantum mechanical (Fig. 30.6) and is determined by the distance of closest approach for the classical electron trajectory around an ion. From the trajectory, an effective e-i Coulomb logarithm $\ln\Lambda_{\mathrm{ei}}$ was calculated using Eq. (18), and Eq. (13) was then used to determine $\ln\Lambda_{\mathrm{ib}}$. To bridge the classical and quantum-mechanical regions, the results of Williams and DeWitt[9] were used. For moderate-Z plasmas, where the approximation $\Lambda_{\mathrm{ei}} >> 1$ is applicable, a previously calculated expression[10] was used for $\ln\Lambda_{\mathrm{ei}}$.

However, at high Z, the calculation of $\ln\Lambda_{\mathrm{ei}}$ does not permit approximations based on $\Lambda >> 1$ or the use of λ_{D} as the shielding length (Fig. 30.6). We have extended the calculation into the high-Z region by using the NLDH model. The dominant high-Z effect is that neighboring ions are strongly repelled at distances smaller than the average-ion radius R_o. The NLDH model was found to reproduce results for $\ln\Lambda_{\mathrm{ei}}$ at high Z (as calculated from the uniform electron model), and to also merge smoothly to moderate-Z results (calculated by Liboff[10]). Use of Eq. (13) to relate the average of $\ln\Lambda_{\mathrm{ib}}$ over all ion configurations to the result obtained from an average, spherical, electrostatic potential is probably the greatest source of uncertainty in the calculation, and the resulting error requires further investigation.

Results for $\ln\Lambda_{\mathrm{ib}}$ are shown in Fig. 30.9 at $n_e = 9 \times 10^{22}\ \mathrm{cm}^{-3}$ for $T = 1$ keV, and in Fig. 30.10 for $T = 0.5$ keV. A good fit to the numerical results for all Z is given by Eq. (22). The calculation supports the use of replacing λ_{D} by R_o as the effective shielding distance, Eq. (3b), whenever $\lambda_{\mathrm{D}} < R_o$. The nonlogarithmic term 1.25 in Eq. (24) represents a 50% correction at high Z.

ACKNOWLEDGMENT

This work was supported by the U.S. Department of Energy Office of Inertial Fusion under agreement No. DE-FC08-85DP40200, and by the Laser Fusion Feasibility Project at the Laboratory for Laser Energetics, which has the following sponsors: Empire State Electric Energy Research Corporation, General Electric Company, New York State Energy Research and Development Authority, Ontario Hydro, and the University of Rochester. Such support does not imply endorsement of the content by any of the above parties.

REFERENCES

1. Examples of lnΛ are contained in *NRL Plasma Formulary*, edited by David L. Book (Naval Research Laboratory, Washington, DC, 1983); T. W. Johnston and J. M. Dawson, *Phys. Fluids* **16**, 722 (1973).
2. J. Dawson and C. Oberman, *Phys. Fluids* **5**, 517 (1962).

3. R. S. Cohen, L. Spitzer, and P. Routly, *Phys. Rev.* **80**, 230 (1950).
4. J. Albritton, Laser Program Annual Report 84, UCRL-50021-84 (Lawrence Livermore National Laboratory, Livermore, CA, 1984), pp. 3-50.
5. S. Ichimaru, *Basic Principles of Plasma Physics* (W.A. Benjamin, MA, 1973).
6. D. Bohm, *Quantum Theory* (Prentice Hall, NJ, 1951), pp. 551-555.
7. R. Cauble and W. Rozmus, *Phys. Fluids* **28**, 3387 (1985).
8. W. B. Hubbard and M. Lampe, *Astrophys. J. Suppl. Ser.* **18**, 297 (1969).
9. R. Williams and H. DeWitt, *Phys. Fluids* **12**, 2326 (1969).
10. R. Liboff, *Phys. Fluids.* **2**, 40 (1959).
11. R. Cowan and J. Kirkwood, *J. Chem. Phys.* **29**, 264 (1958).
12. S. Skupsky, *Phys. Rev. A* **21**, 1316 (1980).
13. (a) H. W. Wyld and D. Pines, *Phys. Rev.* **127**, 1851 (1962); (b) The formalism of Ref. 13(a) was used in: S. Skupsky, *Phys. Rev. A* **16**, 727 (1977).
14. J. Dawson, in *Advances in Plasma Physics*, edited by A. Simon and W. B. Thompson (Wiley, NY, 1969), Vol. I, p. 1.
15. As quoted in: I. Shkarofsky, T. Johnston, and M. Bachynski, *The Particle Kinetics of Plasmas* (Addison-Wesley, MA, 1966), p. 233.
16. H. Goldstein, *Classical Mechanics* (Addison-Wesley, MA, 1965), Chap. 3.
17. M. Lamoureux, I. J. Feng, R. H. Pratt, and H. K. Tseng, *J. Quant. Spectrosc. Radiat. Transfer* **27**, 227 (1982).

Section 2
ADVANCED TECHNOLOGY DEVELOPMENTS

2.A Studies of New Geometries for X-Ray Lasers

Laser-produced plasmas have been extensively used as suitable media for soft x-ray lasers. Recently, amplified spontaneous emission at the 130-Å to 200-Å range has been observed in experiments involving laser-produced plasmas.[1-3] Gain coefficients of about 5 to 6 cm^{-1} were measured on $2s^22p^53s$ – $2s^22p^53p$ transitions in neon-like selenium, yttrium, and molybdenum. In the lasing scheme used in these experiments, free electrons in the laser-produced plasma collide with neon-like ions, exciting $2p$ electrons to the $3p$ and $3s$ states (see Fig. 30.11). The $3s$ state decays to the ground level much faster than the $3p$ state, creating a population inversion between the $3s$ and $3p$ states.[4] Stimulated x-ray emission, initiated by slower spontaneous decay from the $3p$ to the $3s$ state, propagates and is amplified along the axis of the plasma (typically 1- to 3-cm long).

In x-ray laser schemes, the target and the irradiating laser parameters should be chosen to maximize population inversion and therefore gain. The gain coefficient depends mainly on the plasma temperature and density and on the nuclear charge Z of the target material. The temperature (which in turn depends on the incident laser irradiance) determines the various atomic rates and the fraction of neon-like ions. For a given neon-like ion fraction, the gain increases with the plasma electron density until that density is high enough to allow electron collisions to equilibrate the level populations, thus reducing the population inversion and therefore the gain. The electron density corresponding to the peak gain increases with the nuclear

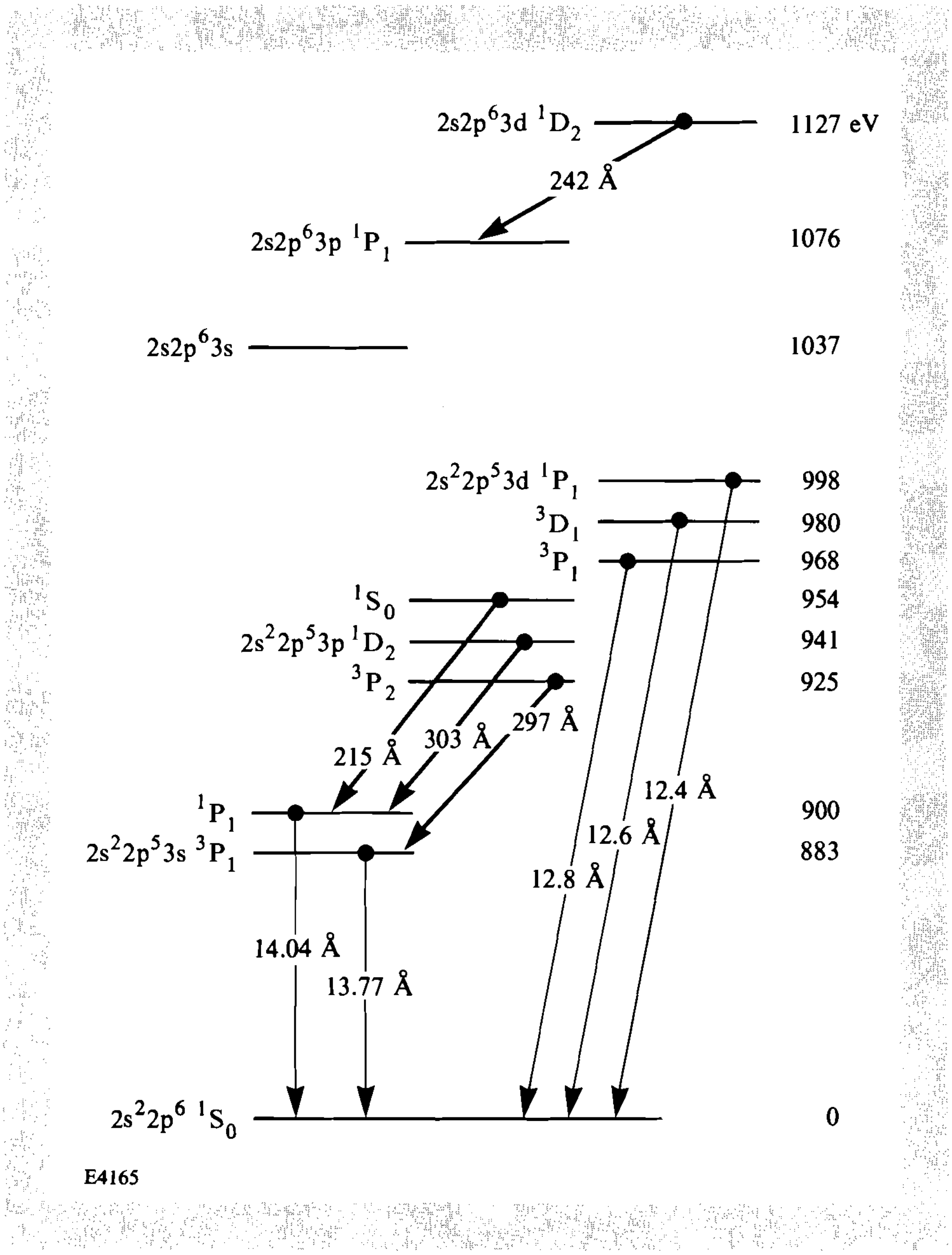

Fig. 30.11
The x-ray and XUV transitions in Ne-like nickel. The XUV transitions that are expected to exhibit gain are emphasized. The five $n=3$ to $n=2$ x-ray lines shown are those used to diagnose the fraction and spatial extent of Ne-like ions in the plasma.

charge Z; it is about 10^{21} cm^{-3} for iron ($Z = 26$) and 10^{22} cm^{-3} for krypton ($Z = 36$).[5] For a given density, the gain initially increases sharply with increasing nuclear charge Z, then decreases slowly. Thus, for each density value there is an optimal Z.

It should be mentioned that for lower-Z plasmas, the opacity of the $2s$-$2p$ transitions transverse to the lasing direction is higher and has to be more carefully controlled since it can reduce the gain by increasing the population of the lower laser level.

We chose nickel as the lasing medium because, for the density range attained in these experiments (in the mid-10^{20} cm^{-3}), it yields a gain coefficient close to optimal. Also, nickel requires only modest plasma temperatures (500 to 700 eV) as compared with a higher-Z target. This temperature is compatible with the laser intensity available for these experiments. For lower-Z ions, the lower laser power dictated by the requirement of a lower temperature may be inadequate for achieving burn-through and desirable density profile characteristics. Choosing nickel (rather than selenium) leads to longer-wavelength lasing lines, in the range 215 to 300 Å, as compared with 180 to 210 Å for selenium. Since the optimal plasma density (even for nickel) is higher than that occurring in simple exploding-foil experiments, we have concentrated on new target geometries that can increase the plasma density and lead to higher gain.

In previous x-ray laser experiments,[1-3] thin exploding targets were used to avoid the steep density gradient characteristic of plasma expansion from thick targets. The thin target explodes and generates a roughly cylindrical plasma having a flat electron density profile of about 3-5 $\times$ 10^{20} cm^{-3}, and a flat temperature profile. Since the lateral scale length is of the order of 100 to 150 μm, the refraction effect is reduced, and rays can now propagate 1 to 2 cm in such a profile before being deflected out of the lasing region.

The exploding foil geometry suffers from two drawbacks: first, in order to achieve a symmetrically expanding plasma with a long scale length, the laser must burn through the foil before the peak of the laser pulse. Consequently, the electron density at the time of lasing is only about 4 $\times$ 10^{20} cm^{-3}. This is lower than the density for maximum gain coefficient by at least a factor of 2. Second, the refraction effect, which was reduced by employing the exploding foil geometry, still limits the length of the plasma column to 1 to 3 cm because the density profile tapers away from the axis. In the new geometries described here, an attempt is made to overcome these limitations. These geometries, in addition to increasing the density, may also result in a wider lasing channel and a concave lateral density profile, both of which reduce refraction losses.

In the following section we introduce these new geometries and discuss their expected performance. We then present experimental results, accompanied by computer simulations, and discuss their relevance to future x-ray laser experiments.

New Geometries: Theoretical Considerations

1. Two Exploding Foils

The density profile of a single, thin, exploding nickel foil is shown schematically in Fig. 30.12(a). After the initial burn-through, a nearly symmetrical expansion, with a Gaussian density profile, is obtained. A population inversion is achieved early, but the lasing x rays suffer severe refraction losses until the plasma has reached large enough lateral dimensions. Since the optimal temperature for lasing in neon-like nickel is about 600 eV (compared with about 1 keV for selenium), a lower irradiance is used. This leads to a lower ablation rate and dictates using a thinner foil. A thinner foil, in turn, leads to a smaller density scale length. For single-foil geometry, the only way to overcome this drawback is to employ much longer laser pulses with thicker foils.

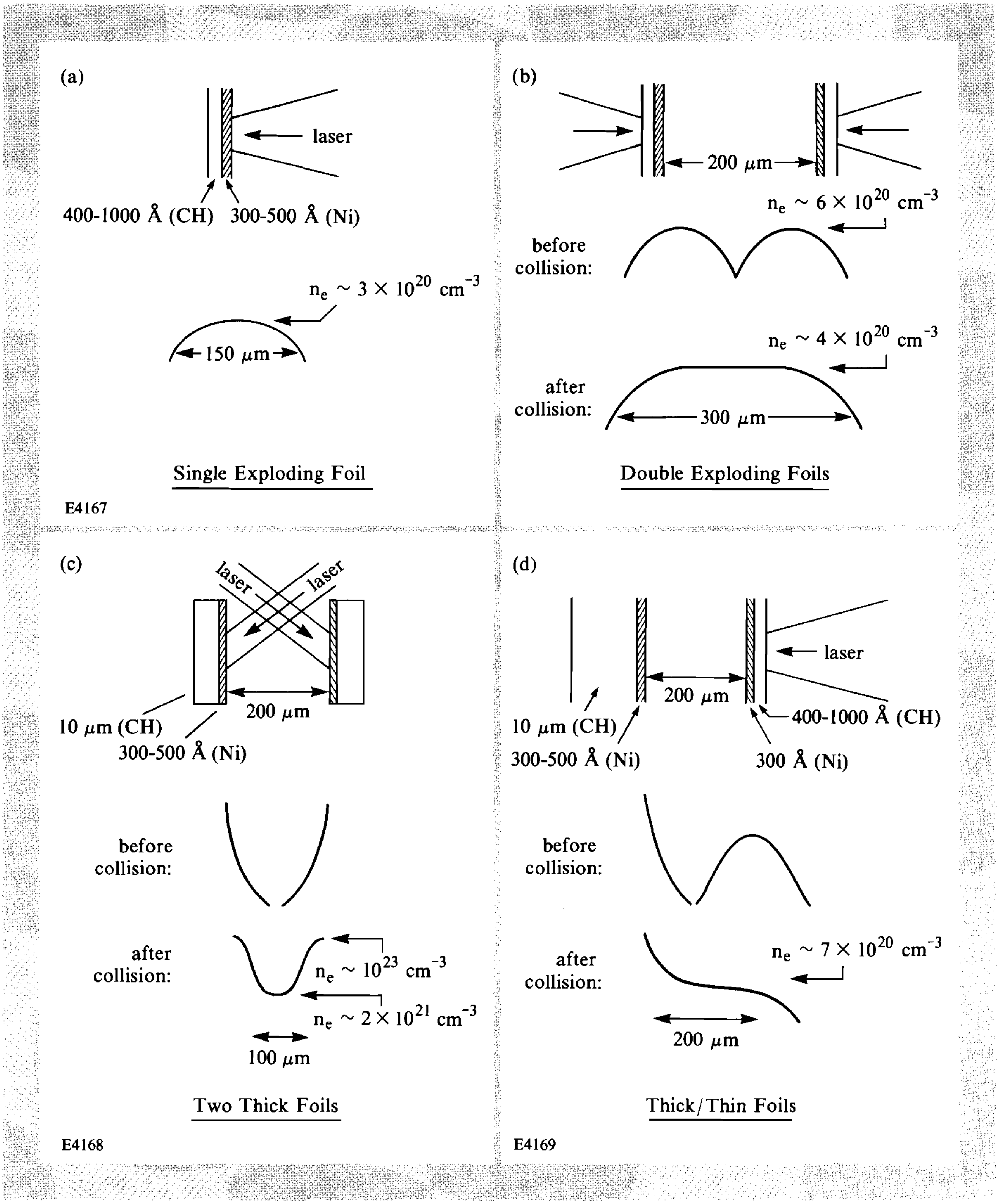

Fig. 30.12
The conceptual spatial density profile behavior of several target configurations discussed in this report: (a) single exploding foil; (b) double exploding foil; (c) two thick foils; and (d) a combination of one thick and one thin foils.

An improved arrangement is that of two parallel foils facing each other[6] as shown in Fig. 30.12(b). This is in contrast to a recently suggested geometry in which the foils are placed next to each other along their edges (thus forming a slit),[7] rather than facing each other. In the former geometry, the lasing medium is formed by the bulk of the expanding plasma, while in the slit geometry it is formed only from the plasma created on the slit edges. The optimal distance between the exploding foils was found to be about 150 to 250 μm, for an irradiance of the order of 10^{13} W/cm^2. For much larger distances, the collision between the two plasmas occurs when the density has fallen to too low a level for lasing, whereas for much smaller distances the increase in scale length over the single-foil case is not significant.

The arrangement of two exploding foils offers the following advantages: first, when the plasmas expand inward from the two foils and begin to collide, a concave density profile having a dip at the midplane is formed. Later on, the profile is flat topped with a greater width than in the corresponding single-foil case. Additionally, we have found that a pair of thin foils can be irradiated from only one side and still result in density profiles similar to the case where a double foil is irradiated from both sides. In such a design, the laser burns through the first foil prior to the peak of the pulse; it is then transmitted through the first-foil plasma and absorbed by the second foil, causing it to explode. A uniform plasma can be formed between the foils even though the interface between the two colliding plasmas will not be on the midplane. The thicknesses of the two foils can be optimized in order to produce more uniform temperature and density profiles. This requires that the energy absorbed in the second foil be higher than that absorbed in the first foil to compensate for the time delay between the two foil explosions. The related geometry of imploding thin cylindrical shells has been previously studied at the Laboratory for Laser Energetics, theoretically and experimentally.[8] In the cylindrical geometry, the effects of widening the density profile and making it concave apply in both transverse dimensions, rather than in only one of them. However, the cylindrical geometry requires a large number of beams, appropriately positioned to provide uniform illumination of the target.

2. Two Ablating Slabs

The arrangement of two exploding foils does not result in significantly higher plasma density as compared with the single-foil case. This is because when the two foils collide they both are expanding outward. Since the mass is limited in each foil, there is no hydrodynamic support from the two exploding plasmas, and the maximum pressure occurs in the collision region; this leads to a rapid disassembly of the system. To meet the goal of achieving higher density we have designed a novel geometry, consisting of two slabs (thick foils) irradiated on their inner surfaces that face each other [Fig. 30.12(c)]. Since the laser does not burn through these thick foils, the resulting density profile falls sharply from either foil toward the midplane. A concave profile with a minimum between the slabs is formed. The ablated material, which is now hydrodynamically confined between the slabs, reaches densities throughout the pulse about a factor of 10 to 100 times higher than those attained in the exploding-foil geometries. The slab separation can be chosen to yield the optimal density for an extended period of time. A much higher x-ray laser gain can be obtained with this geometry, compared to that of the exploding foils, because of the higher, more optimal density that is achieved and because of the collimating effect of a concave density profile. In this geometry, rays traveling in an off-axis direction will be refracted back into the lasing medium rather than out of it, as in the convex density profile of an exploding foil. The higher density may adversely affect lasing if the transverse opacity of transitions to the ground state becomes much higher than 1. The high opacity repopulates the lower level of the lasing transition, leading to a reduction in the population inversion. This effect can be particularly severe because the stagnated plasma lacks a velocity gradient that could mitigate the effect of opacity (through the Doppler shift). To remedy this problem, the two foils can be made from thin layers of the lasing material deposited on a thick substrate. The substrate material will provide the hydrodynamic confinement and wave guiding without contributing to the population of the lower laser level via resonant excitations.

3. A Pair of Exploding/Ablating Foils

As in the case of the two thin foils, we have found a simpler version of the geometry of two ablative slabs that retains some of the advantages of that particular geometry. In this simplified version, a thin foil is placed in front of a thick foil and is irradiated by a single laser beam [Fig. 30.12(d)]. The laser irradiates the thin foil, burns through it before the peak of the pulse, and then irradiates the thick foil. The collision between the plasmas of the exploding thin foil and ablating thick foil forms a plateau on the falling density profile of the thick foil. The resulting density is higher than that attained in exploding-foil plasmas. The scale length of this plateau is about equal to the original foil separation. The advantage of high density, inherent in the thick-foil case, is partially retained. However, the advantage associated with a concave density profile is retained now only for rays traveling toward the thick foil.

Experimental Studies and Numerical Simulations

The new geometries for x-ray-laser targets described in the preceding section were tested on the glass development laser (GDL) single-beam laser system. In all cases the target material was nickel. We have not attempted actual gain measurements because the line-focus lens at our disposal had a length of only 1.5 mm. However, this length was sufficient for studying the hydrodynamic behavior of the proposed new geometries. In the coming months we intend to perform experiments using 1- and 2-cm line-focus lenses, which should yield measurable gain.

The targets were irradiated by 600-ps pulses of 527-nm laser light at intensities of a few 10^{13} W/cm^2. A green-wavelength laser is more suitable than a blue-wavelength laser for exploding-foil experiments because with the shorter wavelength the plasma becomes highly underdense and absorbs less. In the nonexploding geometries, shorter-wavelength illumination is preferable. A cylindrical corrector lens was fitted onto the f/3 spherical focusing lens to provide a line focus 1.5-mm long and about 50-μm wide at the best focus position. Since a small width may give rise to two-dimensional (2-D) plasma expansion, which would severely degrade the density and temperature profiles, we defocused the beam to yield a width of about 120 μm (at widths larger than 120 μm the intensity distribution across the width is not uniform with the present laser conditions).

Planar nickel foils and slabs were used to construct the target geometries described in the preceding section. The thin foils were 300-Å-thick to 800-Å-thick layers of nickel, supported by Formvar ($C_{11}H_{18}O_5$) substrates 400-Å thick. Such substrates have a very small mass compared with that of the nickel foil and will scarcely affect the hydrodynamic behavior of the foil.

An x-ray crystal spectrometer equipped with a 12-μm entrance slit was used to measure the spatially resolved Ni spectra from these targets in the 7-Å to 14-Å range. The spatial resolution is in the direction perpendicular to the foil plane, which is along the distance between the two foils. These spectra can be used to determine the

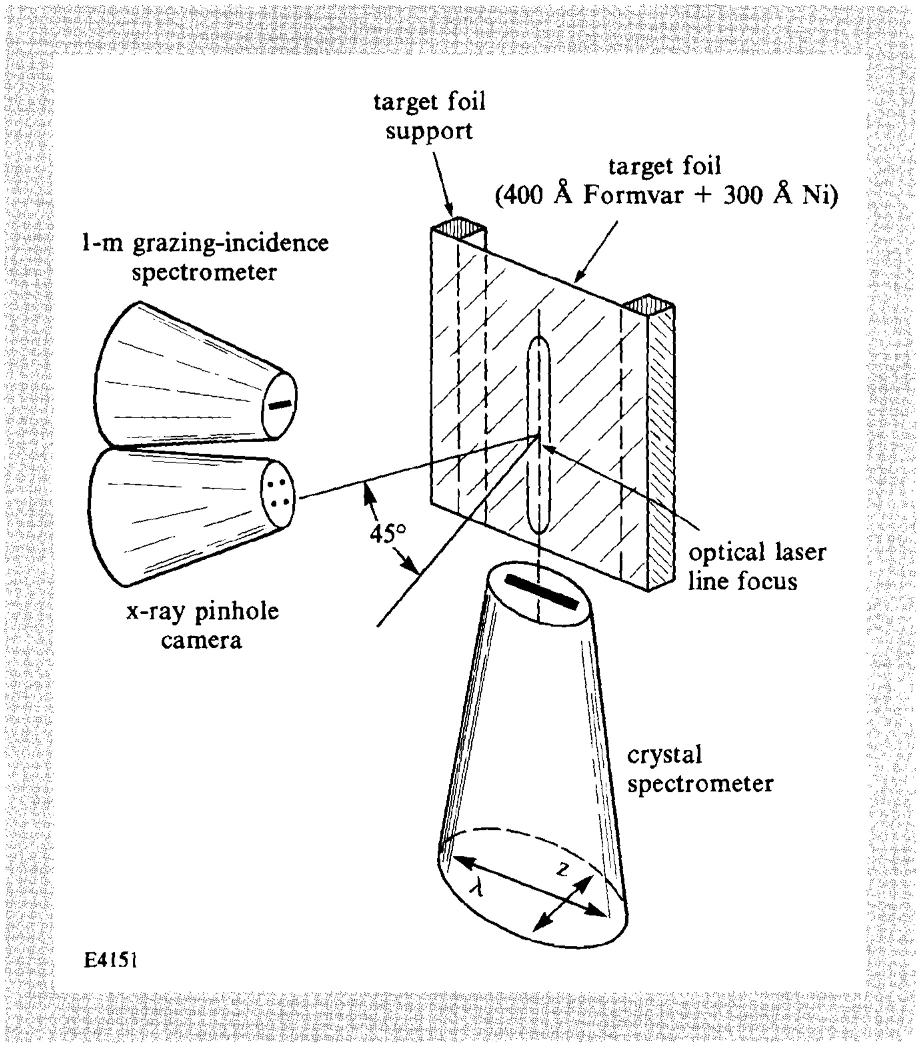

Fig. 30.13
Experimental configuration used for x-ray laser target studies in the GDL target chamber. The crystal spectrometer views the end of the line focus from the bottom. The x-ray pinhole camera and XUV spectrometer view the irradiated side of the target.

plasma temperature and density. Additionally, we used a pinhole camera to measure the focal spot characteristics and also to observe the two-dimensional plasma behavior (along the line focus direction and normal to that direction). This information is important in evaluating the hydrodynamic performance of the new geometries. The XUV spectra in the 40-eV to 250-eV range were measured using a 1-m grazing incidence spectrograph. This spectral range contains the lines that are predicted to lase when using longer line-focus irradiation. Finally, time-resolved measurements of the laser light transmitted through the target were made in order to determine the occurrence of timely burn-through, which is necessary for the formation of a flat density profile.

Figure 30.13 shows the experimental arrangement. The incident laser propagates horizontally and the line focus is oriented vertically. The crystal spectrometer views the plasma along the axis of the line focus. The pinhole camera and XUV spectrometer view the front (irradiated) side of the target at 45° to the normal. The laser light that is transmitted through the target is collected by a spherical *f*/3 lens. The image of the target (along the line focus) is relayed to the slit of a streak camera to obtain time resolution of the transmitted light.

Figure 30.14 shows a typical x-ray spectrum obtained from a thick (about 100-μm) nickel target irradiated at 1 × 10^{13} W/cm^2. To calibrate the wavelength scale we used a target composed of two

Fig. 30.14
A sample x-ray spectrum from a thick nickel target. The lines designated by letters *a* through *e* are the $n = 3$ to $n = 2$ lines of Ne-like nickel. The lines *f* and *g* are due to $n = 4$ to $n = 2$ transitions. Also indicated are the F-like nickel transitions used in this work. The incident laser intensity was 10^{13} W/cm^2.

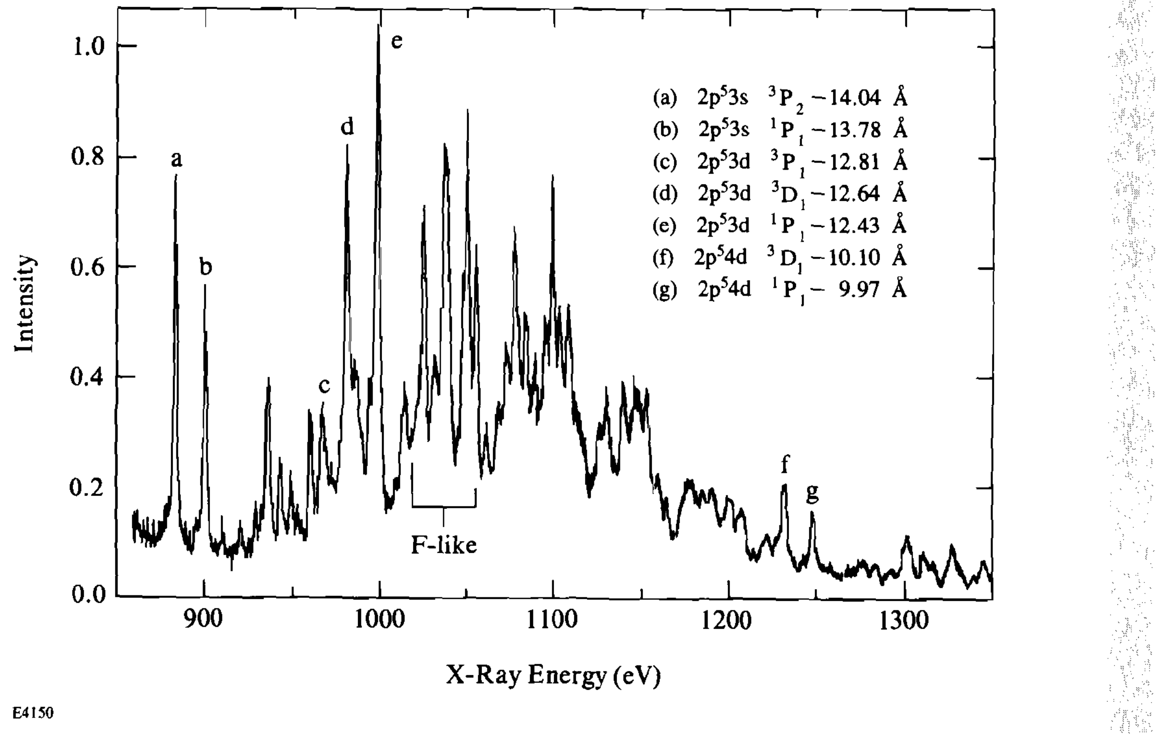

regions: nickel and Teflon, irradiated by a line focus. On a spatially resolved spectrum, lines of nickel and fluorine are juxtaposed, thereby providing a reference wavelength scale. Figure 30.14 shows lines from the NiXIX to NiXXII states of ionization (Ne-, F-, O-, and N-like ions). The individual Ne-like and F-like lines can be distinguished, while the emission from the other ionization species appear as unresolved transition arrays. The lines labeled in Fig. 30.14 indicate some of the various Ne-like and F-like lines that were identified using a relativistic atomic structure code.[9] We use the relative intensity of the $2p^6$-$2p^5 3s$ and $2p^6$-$2p^5 3d$ resonance transitions in the Ne-like ions and the analogous $2p^5$-$2p^4 3s$ and $2p^5$-$2p^4 3d$ resonance transitions in the F-like ions to estimate the relative fractional population of these species (from which temperature can be inferred).

In order to determine the thickness of Ni foil required for properly timed burn-through, we started by irradiating single exploding foils of various thicknesses. Figure 30.15 shows spatially resolved spectra (isodensity contours) from three Ni foils of different thicknesses; the substrate in these shots only was a 3000-Å-thick CH layer. In all three cases the laser irradiance was about 3 × 10^{13} W/cm^2. In Fig. 30.15, the vertical axis is the spectral direction and the horizontal axis is the spatially resolved direction. The laser is incident from the right. Such results indicate whether the target explosion provides an adequate plasma profile for x-ray lasing. For achieving a flat density profile, the foil has to be burned through before the peak of the pulse; in this case, the time-integrated spectrum should be relatively symmetrical (front to back). For too thick a foil, the spectrum is expected to fall much more sharply toward the back of the foil. The spectra in Fig. 30.15 indicate that the 300-Å nickel foil explodes quite symmetrically, whereas the symmetry is gradually degraded for the thicker foils.

One-dimensional (1-D) computer simulations were performed in slab geometry. Since the extent of plasma expansion is of the order of the laser spot width, it is expected that 2-D effects will not markedly change the target behavior. This assumption has been confirmed by 2-D runs that were performed for some of these geometries. Figure 30.16 shows the spatial temperature and density profiles at the peak of the pulse from the 1-D simulations of all three Ni-foil thicknesses shown in Fig. 30.15. These profiles agree qualitatively with the behavior of the foils as exhibited by the time-integrated, spatially resolved spectra; the thinner foil exhibits flat-top density and temperature profiles, whereas the thicker foils show a sharper falloff. A more quantitative comparison with calculated, time-integrated, spatial x-ray profiles of resonance line emission is now in progress.

Figure 30.17 shows the spatially resolved spectrum from a 300-Å Ni foil (supported by a 400-Å CH substrate) irradiated at 1.25 × 10^{13} W/cm^2. Compared with the spectrum in Fig. 30.15, the use of a lower irradiance and a thinner CH substrate results in a spectrum that shows a higher Ne-like fraction and a more symmetric expansion of the nickel plasma. The experimental results shown in Fig. 30.15 were obtained using a higher irradiance than that required to maximize the Ne-like ion fraction. This is partly due to the use of a relatively thick

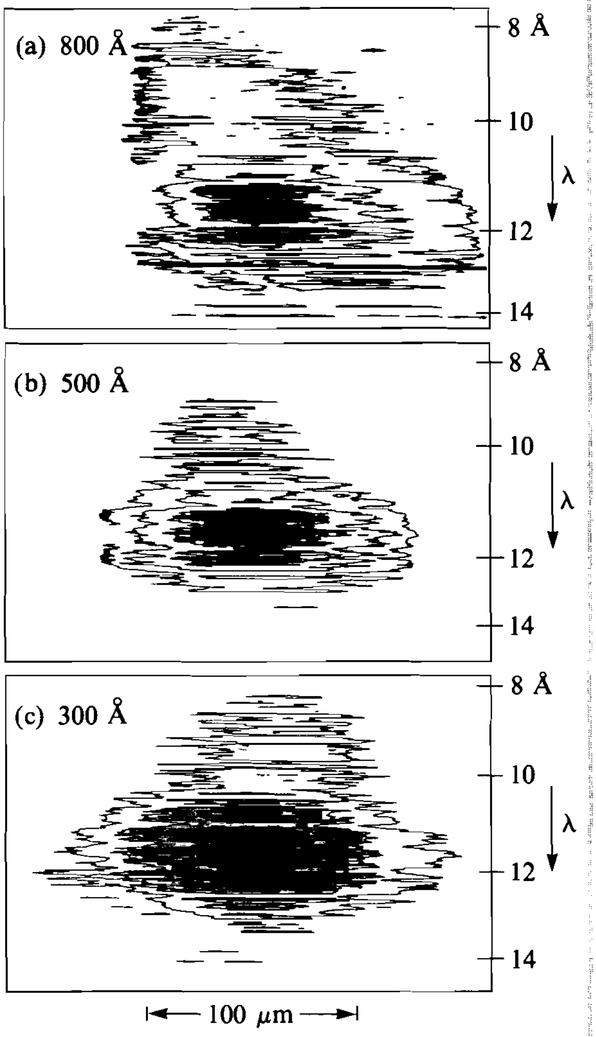

Fig. 30.15
The spatially resolved spectra from three thin-foil targets of various thicknesses: (a) 800 Å Ni, (b) 500 Å Ni, and (c) 300 Å Ni. The spatial axis is transverse to the x-ray laser axis and the wavelength scale is in angstroms, as shown. All targets were supported by 3000 Å of CH and were irradiated by a 0.6-ns pulse at 3 × 10^{13} W/cm^2. In all figures the optical laser is incident from the right side.

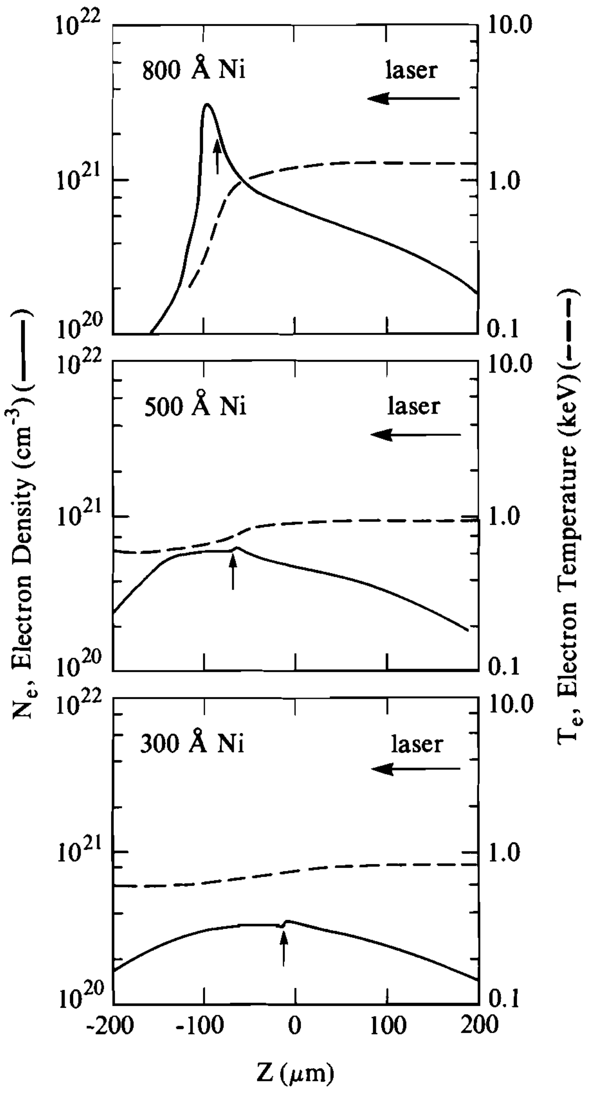

Fig. 30.16
The simulated density and temperature profiles of the targets shown in Fig. 30.15. These profiles are at the peak of a 0.6-ns laser pulse at 3 × 10^{13} W/cm^2. The optical laser is incident from the right. The arrows indicate the plastic/nickel interface in the targets.

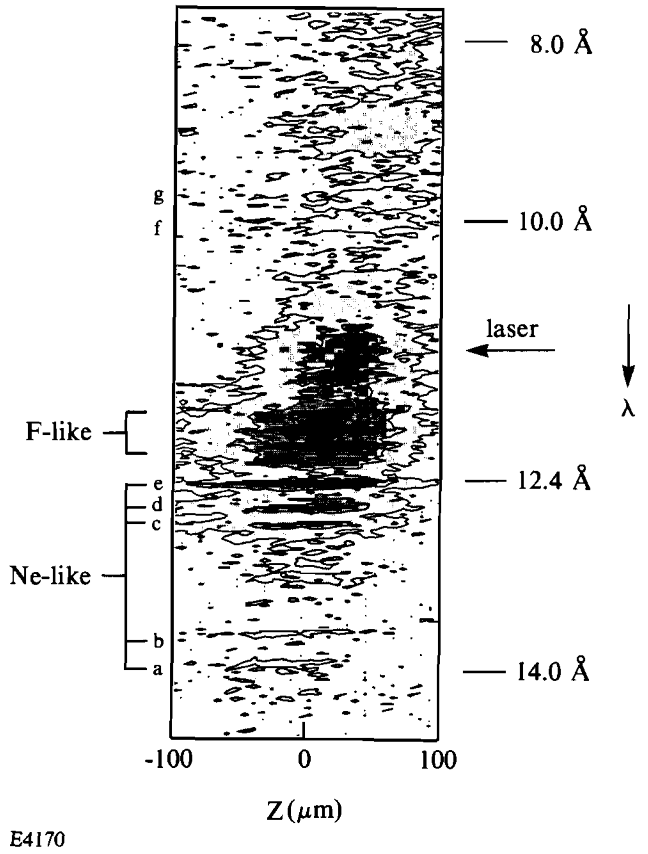

Fig. 30.17
The spatially resolved spectrum of a 300-Å Ni foil (supported by 400 Å Formvar) irradiated by a 0.6-ns pulse at 1.25 × 10^{13} W/cm^2. The expansion of the plasma can be noted in the various lines of the nickel emission. The seven lines labeled *a* through *g* are the Ne-like transitions shown in Fig. 30.14. Also shown are the two F-like lines indicated in Fig. 30.14.

CH substrate. Our numerical simulations, which used a non-LTE, average-ion, atomic physics model to describe the ionization process, have shown that in order to achieve higher Ne-like ionic fraction and still burn through the foil, we need to use a lower laser intensity and a thinner CH substrate. This finding agrees with the experiments.

We next describe two experiments that employ double thin-foil targets irradiated from one side only. Two foil-separation distances were employed: 120 μm and 270 μm. The nickel coatings were over the inside faces.

Figure 30.18 shows the spatially resolved x-ray spectrum for a separation of 120 μm and an irradiation of 1.1 × 10^{13} W/cm^2. The plasma expansion is not greater than that exhibited by the single foil illustrated in Fig. 30.17. In Fig. 30.19, the temperature and density profiles from a simulation of this target are compared. These profiles were obtained at −0.1, +0.2, and +0.4 ns with respect to the peak of the pulse. Figure 30.19 shows that too small a separation distance results in an early collision, leading to a nearly single-foil behavior at later times. A larger separation distance would result in a wider profile. This is particularly important because a single low-*Z* foil with a subnanosecond laser pulse may result in narrower density profile as compared to a higher-*Z* foil (a low-*Z* target requires lower irradiance and thinner foils than needed for higher-*Z* foils).

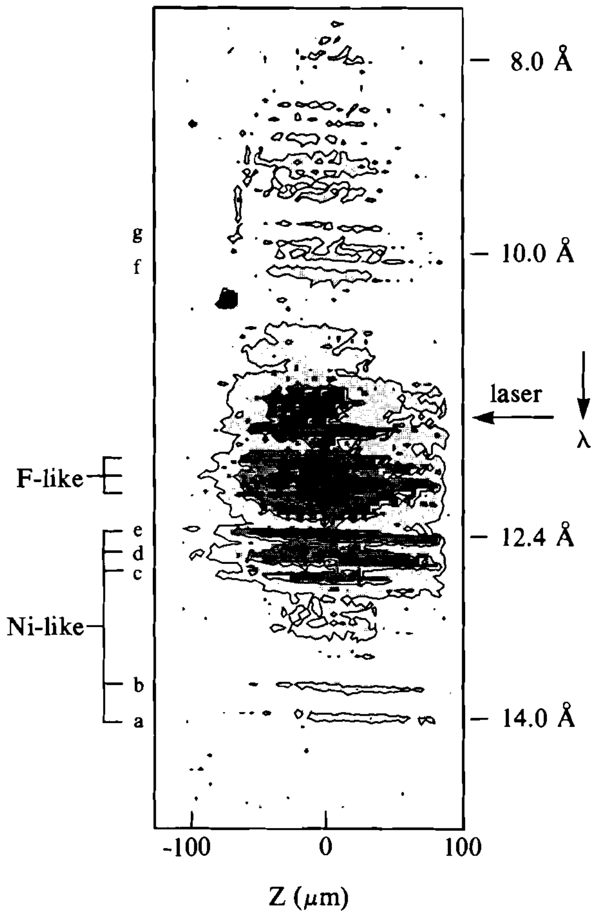

E4171

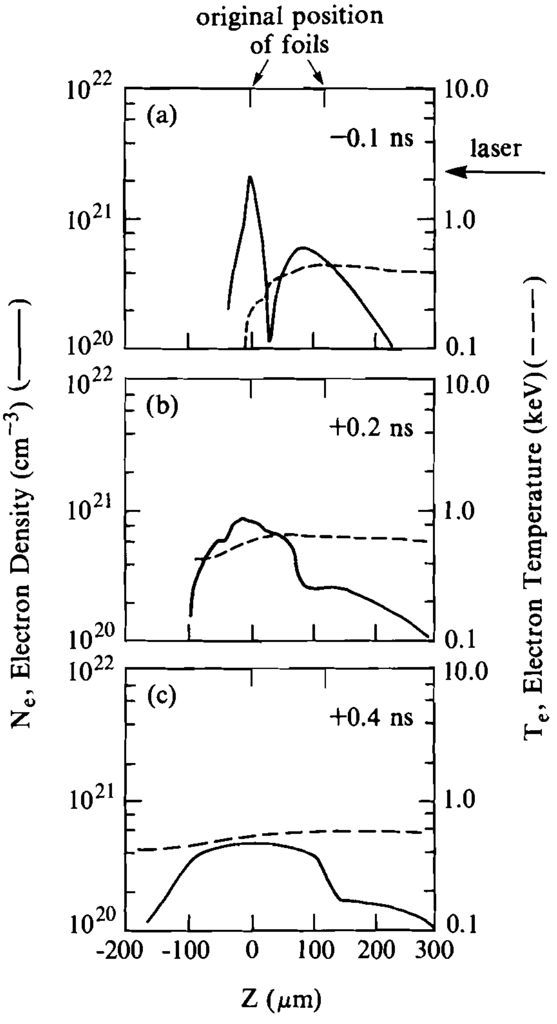

E4172

Fig. 30.18
The spatially resolved spectrum of a double thin-foil target consisting of two 300-Å Ni foils (each supported by 400 Å Formvar) and spaced 120 μm apart. The laser intensity was 1.1 × 10^{13} W/cm^2 in a 0.6-ns pulse.

Fig. 30.19
The simulated density and temperature profiles of the double thin-foil experiment shown in Fig. 30.18 at times (a) −0.1 ns, (b) +0.2 ns, and (c) +0.4 ns, relative to the peak of the pulse. An expansion similar to that of a single exploding foil is observed after the collision.

Figure 30.20 shows the spatially resolved x-ray spectrum from a double thin-foil target with a spacing of 270 μm with a laser irradiance of 1.5 × 10^{13} W/cm^2. These two foils were spaced far enough apart so that the individual foil expansions can be discerned in the x-ray spectral image. The sharp diagonal edge on the left of Fig. 30.20 is caused by the edge of the x-ray film. In Figs. 30.21(a)–30.21(c) we

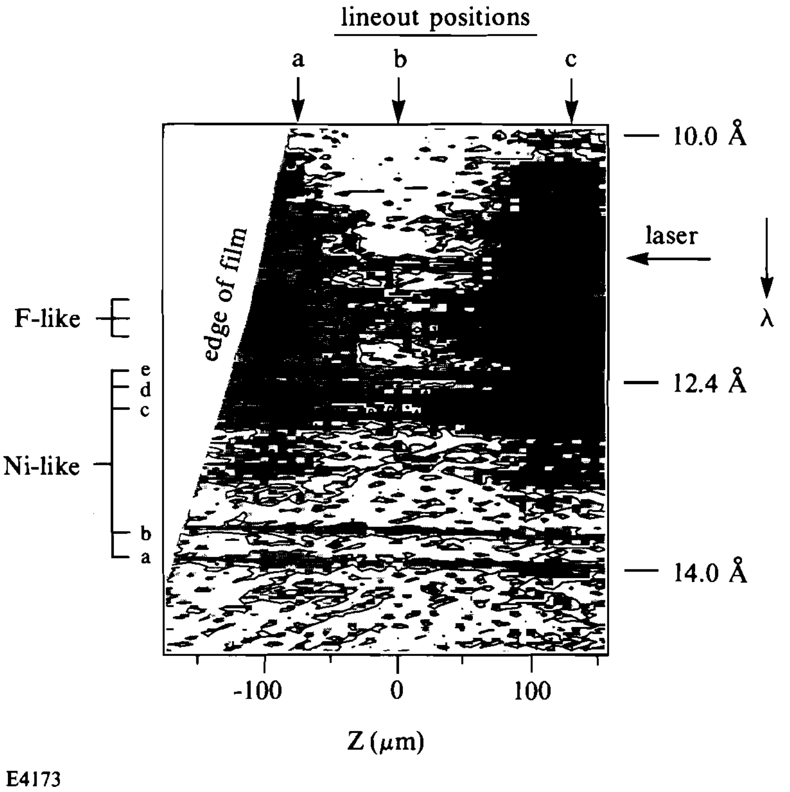

Fig. 30.20
The spatially resolved spectrum of the second double thin-foil target, which consisted of two 300-Å Ni foils (each supported by 400 Å Formvar) spaced 270 μm apart. The laser intensity was 1.5 × 10^{13} W/cm^2 and was incident from the left in the figure. The sections labeled *a*, *b*, and *c* are the lineouts representing the spectra at the rear foil, at the center, and at the front foil, respectively.

show intensity-corrected spectra at the positions marked *a*, *b*, and *c* in Fig. 30.20 (each spectrum has been normalized to the maximum of spectrum *c*). Note that the spectra at *a* and *c* show significant amounts of Ne-like line emission, whereas in the central region the Ne-like line emission is less pronounced. The ratio of F-like to Ne-like line emission was found to be lower in the central region compared to the ratio near the foils, indicating a lower temperature in that region. In addition, the overall lower intensity in the center indicates a lower density there.

Figure 30.22 shows the temperature and density spatial profiles from a simulation of the target with 270-μm spacing. This set of figures displays the profiles at −0.1, +0.3, and +0.6 ns relative to the peak of the pulse. Figure 30.22(a) shows the initial expansions of the two foils, which exhibit a time delay between the expansions of the two foils because the first foil (right side) is initially opaque to the laser light. In fact, the first foil acts as a shutter and blocks the laser light until its intensity is near peak value. Figures 30.22(b) and 30.22(c) correspond to the times when the two plasmas collide and then relax into a long scale-length plasma, respectively. Figure 30.22(b) is shown to illustrate how the two plasmas coalesce; the exact behavior at this point depends on how the collision of two plasmas is modeled. The

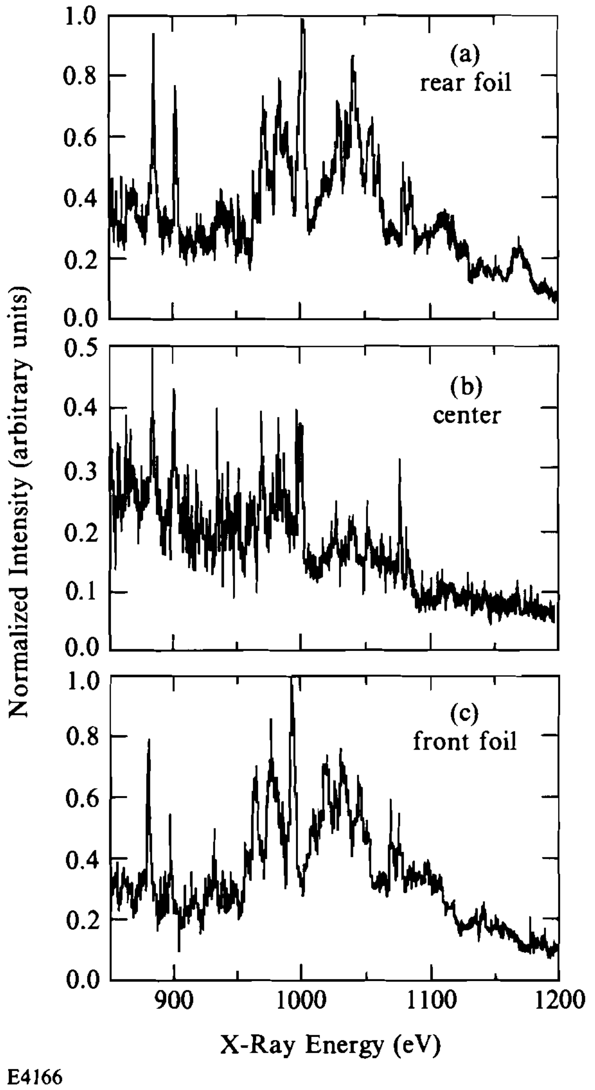

Fig. 30.21
The spectra at various positions in the target shown in Fig. 30.20. The spectra are at (a) the rear foil, (b) the center region, and (c) the front foil. The intensity of each spectrum has been normalized to the peak emission in the spectrum at position *c*. Note that in each foil (spectra *a* and *c*) the spectrum is dominated by Ne-like line emission.

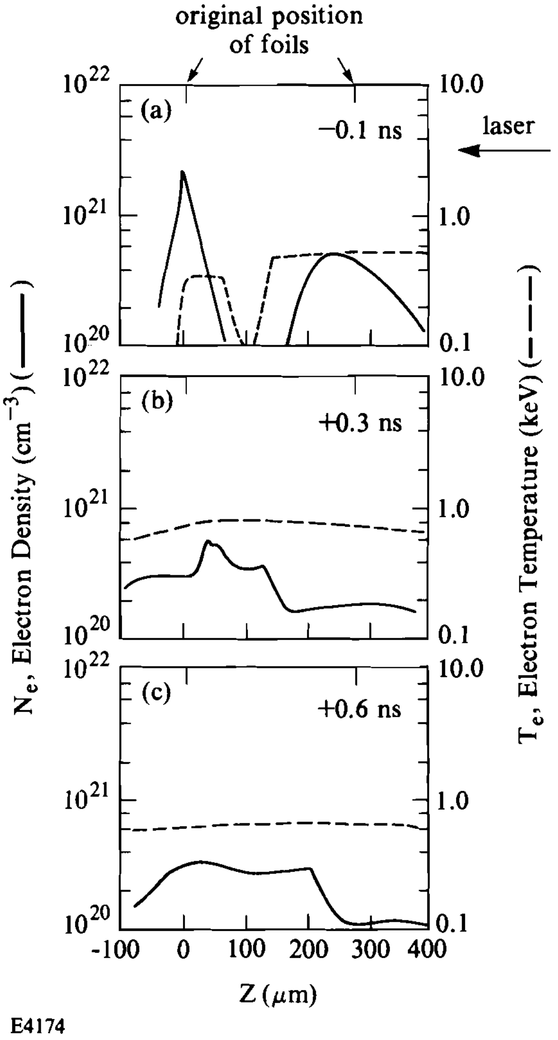

Fig. 30.22
The simulated density and temperature profiles of the double thin-foil experiment shown in Fig. 30.20 at times (a) −0.1 ns, (b) +0.3 ns, and (c) +0.6 ns, relative to the peak of the pulse.

lower measured temperature between the foils can be understood on the following basis: (a) the collision of the two plasmas for this large separation occurs well after the peak of the pulse, when the plasmas are cooler, and (b) 2-D effects, which are important for this foil-separation distance, cause lateral expansion and further cooling.

As mentioned above, one of our goals is to produce a concave density profile of relatively high density. To that end, we studied the behavior of targets that exploit the confinement of an ablated plasma between two thick slabs. Figures 30.23(a)–30.23(d) show the calculated time evolution of the temperature and density profiles for the double-slab target at four different times. In this simulation, the laser light is normally incident on both inner surfaces of the parallel slabs, at an intensity of 1.75 × 10^{13} W/cm^2 on each surface. The figures show the rising density of the plasma, which eventually fills

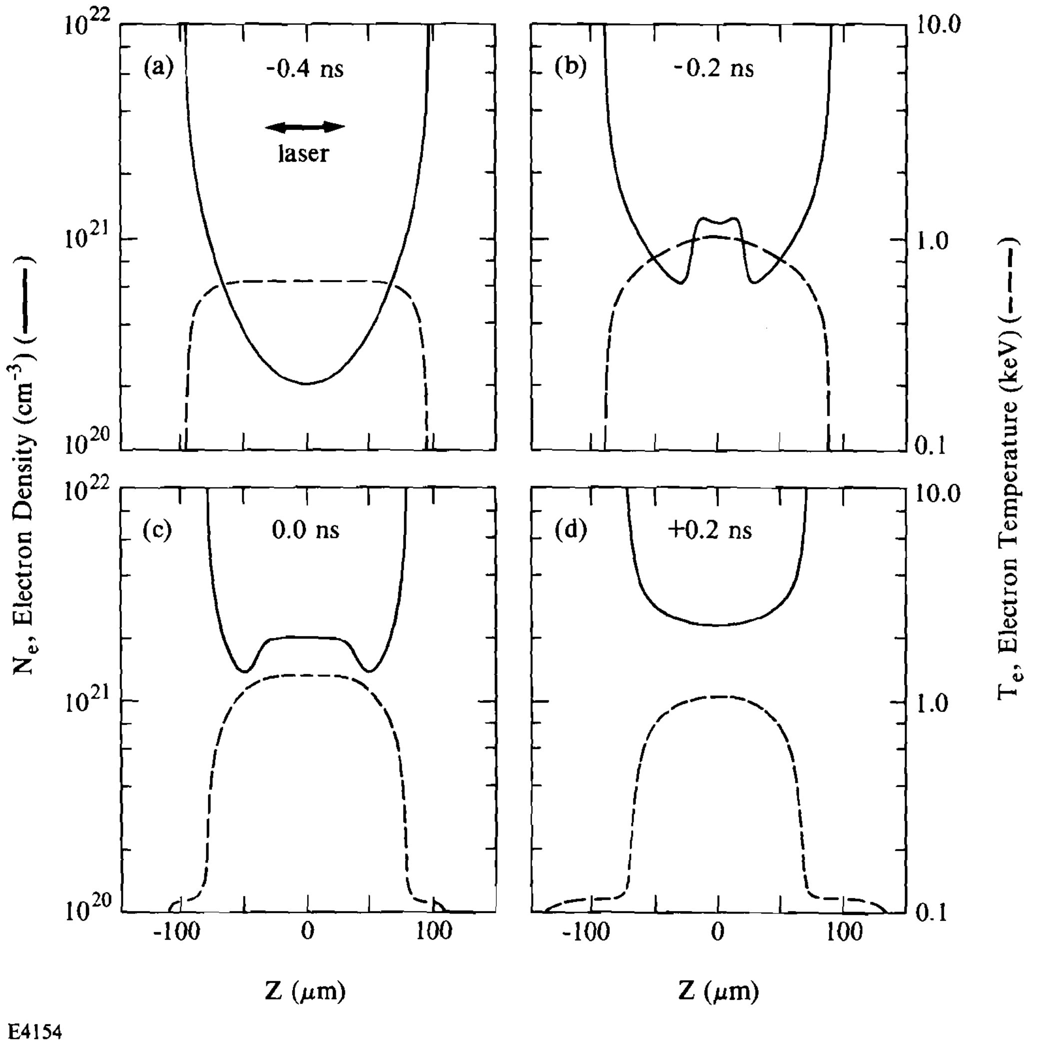

E4154

Fig. 30.23
The simulated density and temperature profiles of the double thick-foil ablative-plasma target shown conceptually in Fig. 30.12(c). The profiles are shown at times (a) −0.4 ns, (b) −0.2 ns, (c) 0 ns, and (d) +0.2 ns, with respect to the peak of a 0.65-ns pulse of 527-nm light at 1.75 × 10^{13} W/cm^2 irradiating each of the two foils. In (b), the collision of the two ablated plasmas begins to increase the density in the interfoil space, followed by a continuously growing density, as seen in (c) and (d).

the interfoil space. The plasma temperature is uniform across the gap at about 1 keV (for nickel, a lower temperature is actually required).

Two simplified versions of this target geometry, suitable for the single-beam GDL experiments, were investigated. The first version involves two thick ($>$100-μm) Ni foils 300 μm apart, one of which was irradiated on its inner surface. Figure 30.24 shows the pinhole camera image of this target, irradiated at about 5 × 10^{13} W/cm^2. The outline of the incident beam is shown for reference, as are the positions of the two slabs. Heating of the inner side of the second foil (by the ablated plasma and possibly by the reflected light from the laser-irradiated foil) can be seen. This preliminary result demonstrates the ability to create a plasma throughout the gap with only one laser beam. Additional studies are under way to optimize this configuration.

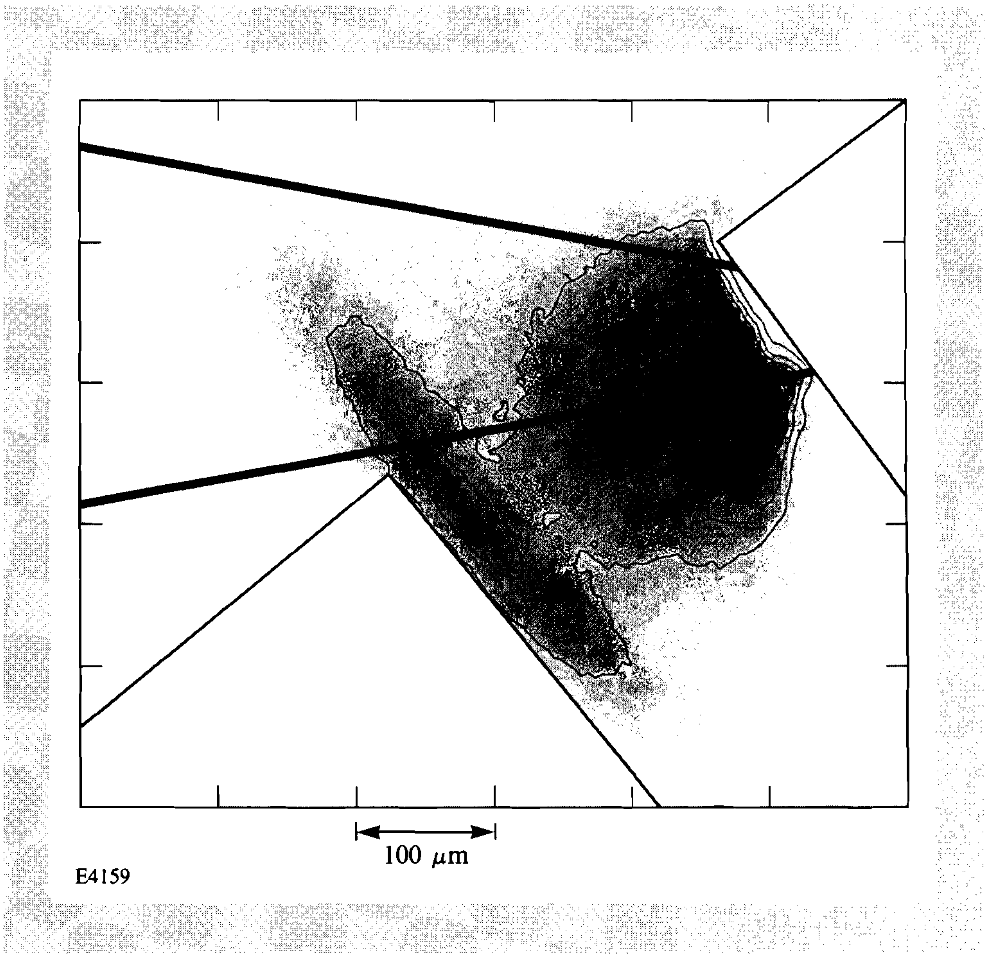

Fig. 30.24
The pinhole image (end on) of a double thick-foil target irradiated by a single laser beam that is incident from the left (the outline of the beam is shown in the figure). The incident intensity is about 5 × 10^{13} W/cm^2. For this image, the pinhole camera was placed in the position of the crystal spectrometer shown in Fig. 30.13.

The second simplified version of the target described in Fig. 30.23 was a combination of a thin (300-Å Ni+ 400-Å CH) foil and a thick ($>$100-μm) Ni foil. The thin foil was positioned with the nickel coating on the side facing the nickel slab. The laser was incident on the outer side (CH support) of the thin foil. Figure 30.25 shows the spatially resolved x-ray spectrum from this target irradiated at 1.5 × 10^{13} W/cm^2. The plasma created by this target has about the same spatial extent as that of the superposition of the observed plasmas from a thin and a thick target separately. The addition of a thin foil in front of a thick foil has the effect of creating a density plateau on the otherwise sharply falling density profile of the thick foil. The ratio of Ne-like to F-like line emission as a function of space indicates that the temperature is approximately constant between the foils and that the increased x-ray emission (due to the addition of the thin foil) is mainly the result of increased density.

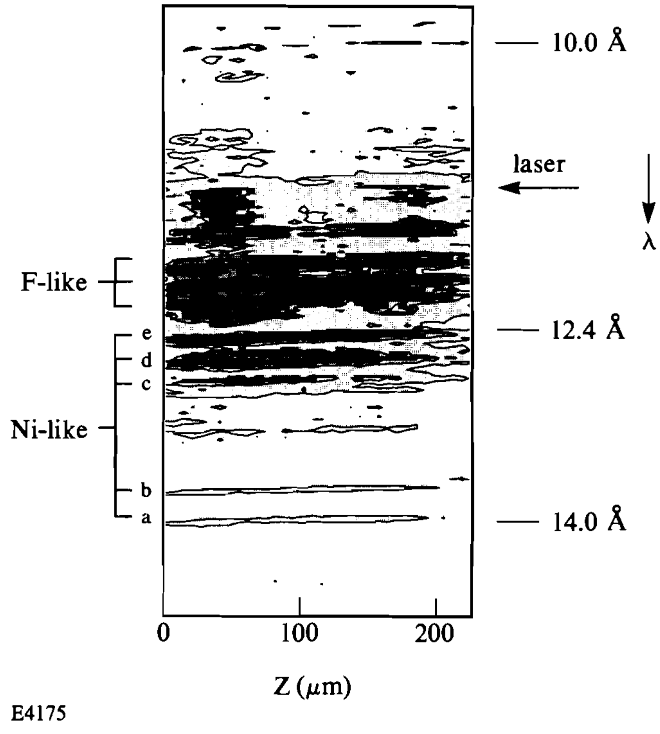

Fig. 30.25
The spatially resolved spectrum of a double-foil target that consisted of a 300-Å Ni foil (supported by 400 Å Formvar) and a 100-μm-thick Ni foil spaced 240 μm apart. The laser intensity was 1.5×10^{13} W/cm^2 and was incident from the right of the figure. A nearly constant emission can be seen in the region between the original foils.

In Fig. 30.26 we show the simulated temperature and density profiles for this target shot at various times relative to the peak of the pulse. They show that the density profile of the ablated plasma from the thick slab is flattened by the presence of the thin exploding foil.

Figure 30.27 summarizes the performance of the new geometries in these experiments. It shows the measured intensity of the Ne-like $2s^22p^6$-$2s^22p^53d$ line (at 12.4 Å) for the various targets described above. All the curves in this figure have the same scale. The laser energy was different in these experiments, but indications from the simulations indicate that the absorbed energy differences were smaller. Comparison of the two lower curves shows that two foils that are too closely spaced behave essentially like a single foil (the slightly wider profile of the single foil can be attributed to the different laser energy). Three features are particularly notable in this figure: (1) the plateau exhibited by the target having one thin and one thick foil; (2) the wide

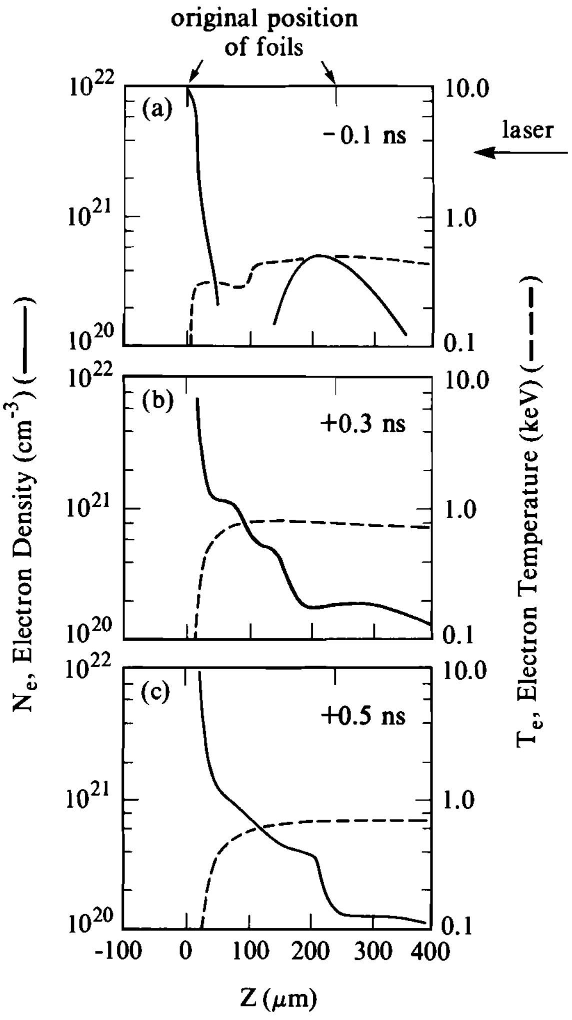

Fig. 30.26
The simulated density and temperature profiles of the double-foil experiment shown in Fig. 30.25. The profiles are shown at times (a) −0.1 ns, (b) +0.3 ns, and (c) +0.5 ns, relative to the peak of the pulse. Noteworthy is the flattened region [(b) and (c)] formed in the density profile from the presence of the single-foil plasma expansion. This behavior is confirmed by the spatially resolved emission shown in Fig. 30.25.

and concave profile in the target having two widely spaced thin foils; and (3) the higher intensity from both of these targets (as compared with a thin target) is indicative of a higher density. These encouraging results should enable the achievement of efficient amplification in future x-ray laser experiments.

ACKNOWLEDGMENT

This work was supported by the Naval Research Laboratory under contract No. N00014-86-C-2281.

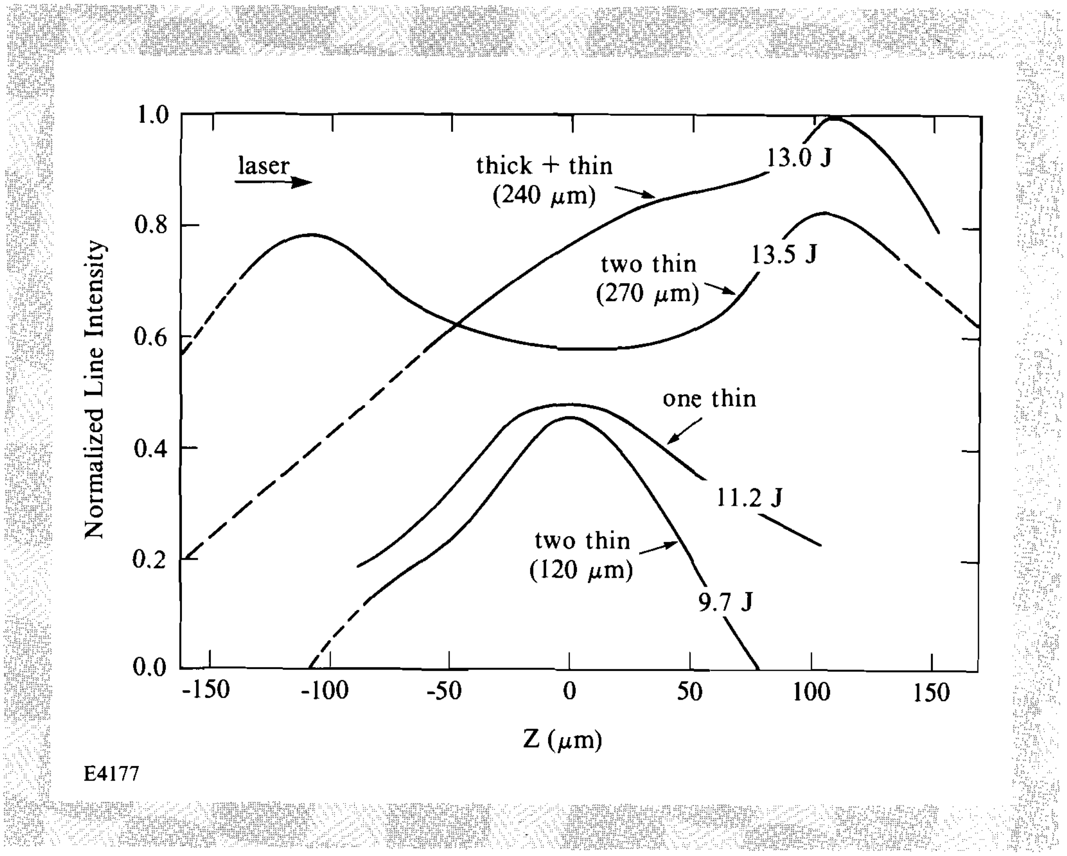

Fig. 30.27
A comparison of the measured intensity of the Ne-like $2s^22p^6$ - $2s^22p^53d$ line (denoted by *e* in Fig. 30.14) for the various targets described above. The curves are plotted on the same scale, but each target has a different irradiated intensity (the laser energy used at each case is specified; the intensity at each case is proportional to the laser energy). This figure shows the relative performance of the various targets to produce large regions of Ne-like ion populations that can be used as x-ray-laser gain media.

REFERENCES

1. M.D. Rosen *et al.*, *Phys. Rev. Lett.* **54**, 106 (1985).
2. D. L. Matthews *et al.*, *Phys. Rev. Lett.* **54**, 110 (1985).
3. Energy and Technology Review, Lawrence Livermore National Laboratory Report UCRL-52000 (1985), p.1.
4. Recently, A. Bar-Shalom of NRCN (Israel) has calculated population inversion on the $2s2p^63d$-$2s2p^63p$ transition (which, for neon-like nickel, is at 242 Å; see Fig. 30.11); here, a $2s$ electron, rather than a $2p$ electron, is excited.
5. U. Feldman, J. F. Seely, and A. K. Bhatia, *J. App. Phys.* **56**, 2475 (1984).
6. M. D. Rosen and P. L. Hagelstein, Lawrence Livermore National Laboratory Report UCRL-94412 (1986).
7. J. P. Dahlburg *et al.*, *Phys. Rev. A* **35**, 2737 (1987).
8. M. C. Richardson, R. Epstein, O. Barnouin, P. A. Jaanimagi, R. Keck, H. Kim, R. S. Marjoribanks, S. Noyes, J. M. Soures,

and B. Yaakobi, *Phys. Rev. A* **33**, 1246 (1986); M. C. Richardson, B. Yaakobi, R. Epstein, J. S. Wark, and J. M. Soures, *High-Intensity Laser Processes* (SPIE, Bellingham, WA, 1986), Vol. 664, p. 270.

9. M. Klapisch *et al.*, *J. Opt. Soc. Am.* **67**, 148 (1977); M. Klapisch, *Comp. Phys. Comm.* **2**, 239 (1971).

Section 3

NATIONAL LASER USERS FACILITY NEWS

National Laser Users Facility (NLUF) activity during the second quarter of FY87 centered on two activities. The first activity was support of experiments being done on OMEGA and GDL. The second activity was a review of proposals for FY88 by the NLUF Steering Committee.

Dr. F. Marshall of LLE is collaborating with **Dr. J. G. Jernigan** from the Space Sciences Laboratory at the University of California, Berkeley, on the development of a two-dimensional active readout array to replace film in an x-ray pinhole camera mounted on the OMEGA target chamber. Data were collected that show an x-ray image from an imploding laser-driven target. These data are being analyzed and an evaluation of the two-dimensional readout array is being made. This work will continue during all of FY87.

Dr. David Bradley from the Lawrence Berkeley Laboratory (LBL) has been collecting data from CH targets containing Al tracer layers with the SPEAXS instrument, in support of **Dr. Burton Henke**'s NLUF experiment. A new filter and two Langmuir-Blodgett multilayer spectral analyzers have been sent from LBL. With these pieces installed into the SPEAXS instrument, the x-ray sensitivity will be extended to energies below 600 eV.

All of the optics needed to steer the GDL beam into **J. Reader**'s (National Bureau of Standards) target chamber are in house. This experiment will use the frequency-doubled output of GDL to study XUV emission from a laser-produced plasma. This experiment will be done during the third quarter of FY87.

The NLUF Steering Committee reviewed the FY88 proposals on 27 February 1987. Members of the Steering Committee are

Dr. Dwight Duston	OSD/SDIO;
Dr. Peter Eisenberger	EXXON Research and Engineering Co.;
Dr. Damon Giovanielli	Los Alamos National Laboratory;
Dr. William Kruer	Lawrence Livermore National Laboratory;
Dr. David Nagel	Naval Research Laboratory; and
Prof. Ravindra Sudan	Cornell University.

The Steering Committee was chaired by **Dr. Bruce Arden** of the University of Rochester. Of the eleven FY88 proposals considered, five were for experiments and diagnostic development related to laser-fusion research, three were for XUV or x-ray studies related to x-ray laser development, two were for experiments related to materials studies, and one was for x-ray microscopy of biological samples. Six of the proposals were for continuation of previous work started at LLE and five were new submissions. Table 30.I contains a list of the considered proposals.

Table 30.I
FY88 NLUF Proposals

No.	Investigator	System	Requested Shots
128	**T. R. Fisher**	OMEGA	30
129	**H. R. Griem**	OMEGA	45
130	**A. A. Offenberger**	OMEGA & GDL	108
131	**J. G. Jernigan**	OMEGA & GDL	10
132	**W. B. McKnight**	GDL	30
133	**J. S. DeGroot**	OMEGA & GDL	200
134	**H. L. Marcus**	GDL	400
135	**U. Feldman**	OMEGA & GDL	60
136	**P. Cheng**	GDL	200
137	**R. R. Whitlock**	GDL	50
138	**C. F. Hooper**	OMEGA	30

U110

ACKNOWLEDGMENT

This work was supported by the U.S. Department of Energy Office of Inertial Fusion under agreement No. DE-FC08-85DP40200.

Section 4
LASER SYSTEM REPORT

4.A GDL Facility Report

GDL continued operation this quarter as a target interaction facility and as the ALPHA backlighting beam. It was also used to study a possible technique to improve on-target laser uniformity. This technique involves firing the beam through a low-pressure inert gas, which fills the BETA target chamber. The results of these experiments are undergoing analysis. The active mirrors were removed from the system this quarter for coating refurbishment and pump module repairs.

A summary of GDL operations for this quarter follows:

Target Shots (BETA)	191
ALPHA Shots	31
Pointing Shots	89
Beamline Test and Calibration Shots	132
TOTAL	443

ACKNOWLEDGMENT

This work was supported by the U.S. Department of Energy Office of Inertial Fusion under agreement No. DE-FC08-85DP40200 and by the Laser Fusion Feasibility Project at the Laboratory for Laser Energetics, which has the following sponsors: Empire State Electric Energy Research Corporation, General Electric Company, New York State Energy Research and Development Authority, Ontario Hydro, and the University of Rochester. Such support does not imply endorsement of the content by any of the above parties.

4.B OMEGA Facility Report

During the second quarter of FY87, OMEGA activities included continuing improvements of the laser system characterization. This effort has focused on quantification of beam profile and attempts to improve it. An extensive series of tests was carried out on the test beam (beamline 6-2) to measure wave-front and phase-front characteristics, to analyze the near, far, and quasi-far field, and to determine on-target beam uniformity at 351 nm. The results of these tests suggested modifications to improve near-term uniformity without disturbing the high-density series of experiments. The tests results also led to long-term plans for better control of the quality of the beam profiles.

Beam characterization has been made more efficient by using x-ray images of the OMEGA beams rather than the cumbersome equivalent-target-plane photographs. X-ray target-plane images were obtained by focusing single beams on large-diameter, gold-coated targets. The x-ray images were then compared to equivalent-target-plane photographs of the test beam. Using x-ray target-plane images has led to more accurate beam profile control from the predriver stage of OMEGA and has permitted the tailoring of the beam profile for improved far-field images of the beam.

All the frequency-conversion crystals of OMEGA have been operated under a new thermal sensing system, in which the phase-matching angle of the cell is adjusted for changes in the ambient laser bay temperature. This new system has led to an overall improvement in the conversion reliability of the conversion cells. This improvement, coupled with the liquid-crystal polarizers positioned before each amplification stage to produce a 1,000:1 contrast circular polarization, has resulted in routinely achieving beam balances of the order of 3%. With an improved scheme for measuring transport optics losses, the same level of beam balance can be achieved on target.

During the quarter a large number of target shots was dedicated to the following internal experimental programs: on-target uniformity; energy partition; coronal physics; high-yield, high-density dot spectroscopy; time-resolved ionization; and through-focus uniformity. External programs for NLUF were also supported.

The ALPHA backlighting beam has undergone further development during this quarter. Synchronism to within 50ps with the OMEGA laser and control over the coincidence time with OMEGA have been achieved. The ALPHA beam has been characterized for profile and focus position on spherical targets within the OMEGA target chamber. Backlighting tests were begun with the ALPHA beam in the shorter (<200-ps) pulse mode.

A summary of OMEGA operations this quarter follows:

Driver Shots	51
Beamline Test Shots	107
Target Shots	248
ALPHA Shots	22
TOTAL	428

ACKNOWLEDGMENT

This work was supported by the U.S. Department of Energy Office of Inertial Fusion under agreement No. DE-FC08-85DP40200, and by the Laser Fusion Feasibility Project at the Laboratory for Laser Energetics, which has the following sponsors: Empire State Electric Energy Research Corporation, General Electric Company, New York State Energy Research and Development Authority, Ontario Hydro, and the University of Rochester. Such support does not imply endorsement of the content by any of the above parties.

PUBLICATIONS AND CONFERENCE PRESENTATIONS

Publications

R. R. Whitlock, S. P. Obenschain, J. Grun, J. A. Stamper, J. A. Sprague, B. V. Sweeney, B. H. Ripin, and R. S. Craxton, "Flash *X* Radiography of Laser-Accelerated Foils," *J. Appl. Phys.* **61**, 131–141 (1987).

B. Yaakobi, O. Barnouin, C. B. Collins, R. Epstein, A. Hauer, S. A. Letzring, F. J. Marshall, R. L. McCrory, M. C. Richardson, J. M. Soures, and S. Wagel, "Laser-Generated X-Ray Studies Relevant to Compression Diagnostics and Nuclear Level Excitation," *Laser Interaction and Related Plasma Phenomena*, edited by H. Hora and G. M. Miley (Plenum Press, NY, 1986), Vol. 7, pp. 89–108.

M. C. Richardson, P. W. McKenty, F. J. Marshall, C. P. Verdon, J. M. Soures, R. L. McCrory, O. Barnouin, R. S. Craxton, J. Delettrez, R. J. Hutchison, P. A. Jaanimagi, R. Keck, T. Kessler, H. Kim, S. A. Letzring, D. M. Roback, W. Seka, S. Skupsky, B. Yaakobi, S. M. Lane, and S. Prussin, "Ablatively Driven Targets Imploded with the 24-Beam OMEGA System," *Laser Interaction and Related Plasma Phenomena*, edited by H. Hora and G. H. Miley (Plenum Press, NY, 1986), Vol. 7, pp. 421–448.

M. C. Richardson, G. G. Gregory, R. L. Keck, S. A. Letzring, R. S. Marjoribanks, F. J. Marshall, G. Pien, J. S. Wark, B. Yaakobi, P. D. Goldstone, A. Hauer, G. S. Stradling, F. Ameduri, B. L. Henke, and P. A. Jaanimagi, "Time-Resolved X-Ray Diagnostics for High Density Plasma Physics Studies," *Laser Interaction and Related Plasma*

Phenomena, edited by H. Hora and G. H. Miley (Plenum Press, New York, 1986), Vol.7, pp. 179–211.

J. F. Whitaker, T. Norris, G. A. Mourou, and T. Y. Hsiang, “Pulse Dispersion and Shaping in Microstrip Lines,” *IEEE Trans. Microwave Theory Tech.* **MTT-35**, 41–47 (1987).

J. C. Lee and S. D. Jacobs, “Refractive Index and $\Delta n/\Delta T$ of Cr:Nd:GSGG at 1064 nm,” *J. Appl. Phys.* **26**, 777 (1987).

J. M. Soures, R. L. McCrory, K. A. Cerqua, R. S. Craxton, R. Hutchison, S. D. Jacobs, T. Kessler, J. Kelly, G. Mourou, W. Seka, and D. Strickland, “High Power Laser Research and Development at the Laboratory for Laser Energetics,” *Laser Research and Development in the Northeast* (SPIE, Bellingham, WA, 1986), Vol. 709, pp. 74–87.

M. Guardalben, A. Schmid, M. Loudiana, and J. T. Dickinson, “Photothermal Analysis of Synergistic Radiation Effects in ThF_4 Optical Thin Films,” *Phys. Rev. B.* **35**, 4026–4030 (1987).

U. Feldman, J. O. Ekberg, C. M. Brown, J. F. Seely, and M. C. Richardson, “2ℓ-$3\ell'$ and 2ℓ-$4\ell'$ Transitions in Heliumlike and Hydrogenlike Silicon,” *J. Opt. Soc. Am. B* **4**, 103–104 (1987).

J. O. Ekberg, J. F. Seely, C. M. Brown, U. Feldman, M. C. Richardson, and W. E. Behring, “Spectra and Energy Levels of Cu XXII, Cu XXIII, Cu XXIV, and Cu XXV,” *J. Opt. Soc. Am B* **4**, 420–423 (1987).

H. Kim, “High Power Laser,” *KSEA Letters* **15**, 13–20 (1987).

H. E. Elsayed-Ali, T. B. Norris, M. A. Pessot, and G. A. Mourou, “Time-Resolved Observation of Electron-Phonon Relaxation in Copper,” *Phys. Rev. Lett.* **58**, 1212–1215 (1987).

Forthcoming Publications

The following papers are to be published in the *Proceedings of the 17th Annual Boulder Damage Symposium*, Boulder, CO, October 1985:

K. A. Cerqua, S. D. Jacobs, B. L. McIntyre, and W. Zhong, “Ion Exchange Strengthening of Nd-Doped Phosphate Laser Glass.”

B. Liao, D. J. Smith, and B. L. McIntyre, “The Development of Nodular Defects in Optical Coatings.”

D. J. Smith, B. Krakauer, C. J. Hayden, A. W. Schmid, and M. J. Guardalben, “Yttrium-Oxide-Based Anti-Reflection Coating for High Power Lasers at 351 nm.”

B. Yaakobi, “X-Ray Diagnostic Methods for Laser-Imploded Targets” and “Thermal Transport, Mass Ablation, and Preheat in Laser-Target Experiments,” to be published in the *Proceedings of the Spring College on Radiation in Plasmas,* Trieste, Italy, June 1985 (World Scientific Publishing Co.).

P. Bado, M. Bouvier, and J. S. Coe, "Nd:YLF Mode-Locked Oscillator and Regenerative Amplifier," to be published in *Optics Letters.*

S. H. Batha and C. J. McKinstrie, "Energy Cascading in the Beat-Wave Accelerator," to be published in a special issue of *IEEE Transactions on Plasma Science on Plasma-Based High-Energy Accelerators.*

D. R. Dykaar, R. Sobolewski, T. Y. Hsiang, and G. A. Mourou, "Response of a Josephson Junction to a Stepped Voltage Pulse," to be published in *IEEE Transactions on Magnetics.*

H. L. Helfer and R. L. McCrory, "Some Properties of a Polarized OCP," to be published in *Strongly Coupled Plasmas*, edited by Forest Rogers and Hugh DeWitt (Plenum Press, New York).

G. Mourou, "Picosecond Electro-Optic Sampling," to be published in the *Proceedings of the High Speed Electronics Conference*, Stockholm, Sweden, August 1986.

S. M. Gracewski and R. Q. Gram, "Analysis of Forces on ICF Targets During Ablation Layer Coating," to be published in the *Journal of Vacuum Science and Technology.*

J. S. Wark, R. R. Whitlock, A. Hauer, J. E. Swain, and P. J. Stone, "Shock Launching in Silicon Using Pulsed X-Ray Diffraction," to be published in *Physical Review B.*

K. A. Cerqua, S. D. Jacobs, and A. Lindquist, "Ion-Exchange Strengthened Phosphate Laser Glass: Development and Applications," to be published in the *Journal of Non-Crystalline Solids.*

K. A. Cerqua, A. Lindquist, S. D. Jacobs, and J. Lambropoulos, "Strengthened Glass for High-Average-Power Laser Applications," to be published in the *Proceedings of SPIE's O-E LASE 1987 Conference.*

H. Kim and M. Wittman, "X-Ray Microscopy of Inertial Fusion Targets Using a Laser-Produced Plasma as an X-Ray Source," to be published in the *Journal of Vacuum Science and Technology.*

H. E. Elsayed-Ali and G. A. Mourou, "Phase Transitions in the Picosecond Time Domain," to be published in the *Proceedings of the 1986 Materials Research Society Meeting*, Boston, MA, December 1986.

W. R. Donaldson, "High-Speed, High-Repetition-Rate, High-Voltage Photoconductive Switching," to be published in the *Proceedings of the 2nd Topical Meeting on Picosecond Electronics and Optoelectronics*, Lake Tahoe, NV, January 1987.

G. Mourou, K. Meyer, J. Whitaker, M. Pessot, R. Grondin, and C. Caruso, "Ultrafast Optics Applied to Modern Device Research," to be published in the *Proceedings of the 2nd Topical Meeting on Picosecond Electronics and Optoelectronics*, Lake Tahoe, NV, January 1987.

R. W. Short, W. Seka, and R. Bahr, "Stimulated Raman Scattering in Self-Focused Light Filaments in Laser-Produced Plasmas," to be published in *Physics of Fluids.*

J. Delettrez, R. Epstein, M. C. Richardson, P. A. Jaanimagi, and B. L. Henke, "Effect of Laser Illumination Nonuniformity on the Analysis of Time-Resolved X-Ray Measurements in UV Spherical Transport Experiments," to be published in *Physical Review A*.

R. L. McCrory and J. M. Soures, "Inertially Confined Fusion," to be published in *Applications of Laser Plasmas*, Chapter 7.

M. Pessot, P. Maine, and G. Mourou, "1000 Times Expansion/Compression of Optical Pulses for Chirped Pulse Amplification," to be published in *Optics Communications*.

K. A. Cerqua, J. Hayden, and W. C. LaCourse, "Stress Measurements in SOL-GEL Films," to be published in the *Journal of Non-Crystalline Solids*.

Conference Presentations

K. A. Cerqua, A. Lindquist, S. D. Jacobs, and J. Lambropolous, "Strengthened Glass for High-Average-Power Laser Applications," presented at SPIE's Optoelectronics and Laser Applications in Science and Engineering 1987 Conference, Los Angeles, CA, January 1987.

The following presentations were made at the 2nd Topical Meeting on Picosecond Electronics and Optoelectronics, Lake Tahoe, NV, January 1987:

J. Nees and S. Williamson, "A Technique for Wing-Suppressed IR Sampling."

W. R. Donaldson, "High-Speed, High-Repetition-Rate, High-Voltage Photoconductive Switching."

R. Sobolewski, D. R. Dykaar, T. Y. Hsiang, and G. A. Mourou, "Picosecond Switching in Josephson Tunnel Junctions."

G. A. Mourou, K. Meyer, J. Whitaker, M. Pessot, R. Grondin, and C. Caruso, "Ultrafast Optics Applied to Modern Device Research."

The following presentations were made at the Ballistic Electrons for Transistors Conference, sponsored by the Engineering Foundation, Santa Barbara, CA, March 1987:

G. A. Mourou, "Direct Investigation of Nonequilibrium Transport Using Ultrafast Optical Techniques."

D. R. Dykaar, "Modern Device Characterization on the Picosecond Time Scale."

D. R. Dykaar, R. Sobolewski, G. A. Mourou, and T. Y. Hsiang, "Time-Domain Characterization of Josephson Tunnel Junctions," presented at the American Physical Society Meeting, Baltimore, MD, March 1987.

G. Mourou, "Impact of Ultrafast Optics in High Speed Electronics," presented at SPIE's Novel Optoelectronic Devices Conference, The Hague, Netherlands, March/April 1987.

The following presentations were made at the American Physical Society Meeting, New York City, NY, March 1987:

R. Sobolewski, D. R. Dykaar, T. Y. Hsiang, C. Vanneste, and C. C. Chi, "Observation of Chaotic Behavior in Josephson Junctions Periodically Kicked by Picosecond Pulses."

J. F. Whitaker, R. Sobolewski, D. R. Dykaar, G. A. Mourou, and T. Y. Hsiang, "Picosecond Pulse Propagation on Superconducting Microstrip and Coplanar Transmission Lines."

ACKNOWLEDGMENT

The work described in this volume includes current research at the Laboratory for Laser Energetics, which is supported by Empire State Electric Energy Research Corporation, General Electric Company, New York State Energy Research and Development Authority, Ontario Hydro, the University of Rochester, and the U.S. Department of Energy Office of Inertial Fusion under agreement No. DE-FC08-85DP40200.